Patient-derived organoids identify an apico-basolateral polarity switch associated with survival in colorectal cancer

Charlotte Canet-Jourdan, Diane-Laure Pagès, Clémence Nguyen-Vigouroux, Jérôme Cartry, Olivier Zajac, Christophe Desterke, Jean-Baptiste Lopez, Emie Gutierrez-Mateyron, Nicolas Signolle, Julien Adam, et al.

© 2022. Published by The Company of Biologists Ltd | Journal of Cell Science (2022) 135, jcs259256. doi:10.1242/jcs.259256

RESEARCH ARTICLE

Patient-derived organoids identify an apico-basolateral polarity switch associated with survival in colorectal cancer

Charlotte Canet-Jourdan[1], Diane-Laure Pagès[1,*], Clémence Nguyen-Vigouroux[1,*], Jérôme Cartry[1,*], Olivier Zajac[2,*], Christophe Desterke[3], Jean-Baptiste Lopez[1], Emie Gutierrez-Mateyron[4], Nicolas Signolle[5], Julien Adam[5], Joel Raingeaud[1], Mélanie Polrot[6], Patrick Gonin[6], Jacques R. R. Mathieu[1], Sylvie Souquere[7], Gerard Pierron[7], Maximiliano Gelli[8], Peggy Dartigues[9], Michel Ducreux[8,10], Valeria Barresi[11] and Fanny Jaulin[1,‡]

ABSTRACT

The metastatic progression of cancer remains a major issue in patient treatment. However, the molecular and cellular mechanisms underlying this process remain unclear. Here, we use primary explants and organoids from patients harboring mucinous colorectal carcinoma (MUC CRC), a poor-prognosis histological form of digestive cancer, to study the architecture, invasive behavior and chemoresistance of tumor cell intermediates. We report that these tumors maintain a robust apico-basolateral polarity as they spread in the peritumoral stroma or organotypic collagen-I gels. We identified two distinct topologies – MUC CRCs either display a conventional 'apical-in' polarity or, more frequently, harbor an inverted 'apical-out' topology. Transcriptomic analyses combined with interference experiments on organoids showed that TGFβ and focal adhesion signaling pathways are the main drivers of polarity orientation. Finally, we show that the apical-out topology is associated with increased resistance to chemotherapeutic treatments in organoids and decreased patient survival in the clinic. Thus, studies on patient-derived organoids have the potential to bridge histological, cellular and molecular analyses to decrypt onco-morphogenic programs and stratify cancer patients.

This article has an associated First Person interview with the first author of the paper.

KEY WORDS: Apicobasolateral polarity, Colorectal cancer, Integrins, Organoids, TGFβ

INTRODUCTION

With one million new cases worldwide every year, colorectal carcinoma (CRC) is the second leading cause of cancer-related death (W.H.O., Globocan 2020; https://gco.iarc.fr). Metastases, seeded by invasive cells, are responsible for almost all deaths from CRC. Despite the heterogeneity of CRCs, invasion and dissemination have principally been studied in the context of the epithelial-to-mesenchymal transition (EMT). This model proposes that carcinoma progression and invasion are associated with the partial or complete loss of epithelial architecture as the EMT transcriptional program is activated to endow cells with migratory and proteolytic activities. Numerous correlative evidence between CRC progression and EMT activation have been found (Brabletz, 2005; Wellner et al., 2009). However, it is still unclear whether this transcriptional program is causative of invasion and metastases formation or if it enables other cell properties, such as stemness or resistance to chemotherapies (Nieto et al., 2016). 3D reconstruction of CRC histological specimens has demonstrated the absence of individual single cells at the tumor margins and point to tumor 'buds' or 'clusters' as the tumor intermediates conquering the invasive front (Barresi et al., 2015; Spaderna et al., 2006; Tsai et al., 2019). Across cancer types, functional studies have proven the predominant participation of collective cancer cell behaviors in the metastatic seeding of secondary lesions (Cheung et al., 2013; Commander et al., 2020; Friedl and Gilmour, 2009; Friedl et al., 2012; Ilina and Friedl, 2009; Ilina et al., 2020). Tumor cell clusters harbor increased migratory fitness and survival capabilities, allowing them to navigate in the peritumoral stroma but also to circulate into the lymphatic and hematogenous systems to reach secondary organs (Aceto et al., 2014; Cheung et al., 2016). However, the mechanisms that fuel the metastatic spread of digestive cancers are under-investigated and understanding the oncogenic pathways and cellular components underlying CRC dissemination remains a major unmet medical need.

The organization of the invading tumor cell clusters varies a lot with cancer types. Analysis of histological specimens from cancer patients has revealed that tumors mostly retain architectural features of the tissue they are originating from at any stage of their metastatic progression. This assessment allows pathologists to identify the type of cancer, independently of the primary or secondary organ location, and points to tissue architecture as a dominant trait of cancers. However, scientific investigations based on the genetic manipulations of animal models have suggested that epithelial apico-basolateral polarity is a tumor-suppressor feature that is lost during carcinoma formation and progression (Bilder, 2004; Bilder et al., 2000). This concept has recently been challenged by the *ex vivo* culture of patient-derived cancer specimens. The analysis of live primary tumor explants from large cohorts of CRC patients monitored *ex vivo* by microscopy provided unexpected findings on cell cluster organization during invasion. These studies revealed a strong collective behavior, an intense epithelial 'addiction', and two

[1]INSERM U-1279, Gustave Roussy, Villejuif F-94805, France. [2]Institut Curie, PSL Research University, CNRS UMR 144, F-75005 Paris, France. [3]INSERM UMR-S-MD A9, Hôpital Paul Brousse, Villejuif F-94805, France. [4]INSERM U-1030, Gustave Roussy, Villejuif F-94805, France. [5]INSERM Unit U981, Experimental Pathology, Gustave Roussy, 94805 Villejuif, France. [6]Plateforme d'Evaluation Préclinique, AMMICA UMS 3655/ US 23, Gustave Roussy, Villejuif F-94805, France. [7]UMR-9196, Gustave Roussy, Villejuif F-94805, France. [8]Department of Medical Oncology, Gustave Roussy, Villejuif F-94805, France. [9]Pathology Department, Gustave Roussy, Villejuif F-94805, France. [10]Paris-Saclay University, Saint-Aubin F-91190, France. [11]Department of Diagnostics and Public Health, University of Verona, Verona 37129, Italia.
*These authors contributed equally to this work

‡Author for correspondence (fanny.jaulin@gustaveroussy.fr)

C.C., 0000-0001-7310-2620; C.D., 0000-0001-7679-2524; E.G., 0000-0003-2074-2354; J.A., 0000-0001-7556-9101; P.G., 0000-0001-6151-4580; S.S., 0000-0002-7768-5293; M.G., 0000-0001-9807-4021; M.D., 0000-0001-8649-7449; V.B., 0000-0001-7086-1920; F.J., 0000-0002-5110-1800

Handling Editor: Andrew Ewald
Received 25 August 2021; Accepted 23 May 2022

Journal of Cell Science (2022) 135, jcs259256. doi:10.1242/jcs.259256

distinct topologies and morphologies in disseminating CRCs depending on their genomic profile (Okuyama et al., 2016). Chromosomal instable cancers, associated with the conventional Lieberkuhnian histological types of CRC, invade while maintaining the apico-basolateral polarity with an inward apical pole ('apical-in') delineating large luminal cavities in the migrating cell cohort (Libanje et al., 2019). In contrast, CRC evolving along the chromosomal stable and hypermethylated pathways spreads as spherical clusters of hundreds of cells that display an inverted 'apical-out' topology with the apical pole surrounding the periphery, in contact with patient fluids and tissues. These tumor intermediates, named 'tumor spheres with inverted polarity' (TSIPs), form in the primary tumor and retain their inverted topology as they invade tissues to initiate metastases in the peritoneum (Zajac et al., 2018). The hypermethylated CRCs arise from serrated precursors lesions and give rise to several histological forms of CRC that are associated with poor patient prognosis. These include mucinous CRC (MUC CRC), the second most frequent type of CRC, associated with an increased secretion of mucins (Jass, 2007).

Here, we combined histological, cellular and molecular approaches from live primary cancer explants and patient-derived organoids to investigate the organization and polarity of MUC CRCs. This study revealed that organoids are useful tools to study tumor invasive behaviors and sensitivity to therapies. We uncovered two subtypes of MUC CRCs, based on a switch in their apico-basolateral polarity orientation, and show that these are associated with distinct patient outcome.

RESULTS

Primary tumor organoids reveal that there is an apico-basolateral polarity switch during the metastatic dissemination of MUC CRCs to the peritoneum

We collected TSIPs from patients with metastatic colorectal carcinoma, and investigated their phenotypes either in suspension or in contact with extracellular matrix. TSIPs were retrieved from the peritoneal effusions at the time of cytoreductive surgery. They were immediately embedded in collagen-I gels, a surrogate for the peritumoral stroma (Wolf and Friedl, 2011). As reported previously, 66% of the TSIPs retained the same inverted apico-basolateral polarity that they displayed in suspension (Zajac et al., 2018). The remaining 34% of TSIPs lost their peripheral apical staining in collagen-I. Instead, basolateral proteins, such as EpCam and E-cadherin, localized at the extracellular matrix (ECM)-abutting membrane (Fig. 1A–C). Concomitantly, a large central cavity formed within the cell cluster (stars, Fig. 1A,C). The enrichment of the actin staining at the membrane outlining the cavity suggested that an apical pole had formed there, which was confirmed by staining for the apical marker ezrin (Fig. 1C). Together, the staining revealed that, although all TSIPs had an inverted apical-out topology in suspension in patient peritoneal effusions, a subset of them reverted their polarity to a conventional apical-in polarity when embedded in collagen-I. To assess whether this could also happen during tissue invasion, we monitored TSIPs invading into peritoneum explants (Zajac et al., 2018). In this assay, we detected TSIPs forming a central lumen outlined with a robust actin staining, reminiscent of the observation made in collagen-I gels (Fig. 1D). To exclude any experimental artifact, we explored the histology of formalin-fixed paraffin-embedded (FFPE) specimens from our patient cohort. Hematoxylin Eosin Saffron (HES) staining identified two distinct histological architectures, which were very homogenous in some patients and consistent with the TSIP phenotype *ex vivo* in collagen-I (Fig. 1E,F). As an example, Patient#6, who had all TSIPs retaining their apical-out topology in collagen-I, presented solid cell masses with an outward ezrin staining, revealing the inverted topology in the metastatic tissue (Fig. 1E,F, top panel). In contrast, Patient#1, who had 79% of TSIPs reverting to an apical-in phenotype in collagen-I, had metastases with a glandular organization, where the apical pole of cancer cell faced large internal luminal cavities (Fig. 1E,F bottom panel). Together, these results show that the unique inverted topology of patient TSIPs in suspension (peritoneal effusions) is maintained in ECM-rich tissues in most cases (apical-out phenotype) (Fig. 1G). However, for a third of the patients, the TSIPs switch to a normal polarity orientation with an inward apical pole surrounding a central lumen (apical-in phenotype).

Apico-basolateral polarity orientation is a cell-autonomous feature of mucinous CRCs

The observations made from patient explants suggested differential polarity orientation in the course of MUC CRC dissemination. Moreover, since tumor architecture correlated with TSIP topology *ex vivo*, both in peritoneum and collagen-I invasion assays, we reasoned that the polarity orientation was a cell-autonomous feature. To validate this hypothesis, we selected three patient-derived xenograft (PDX) mice models from an independent collection of CRCs (Julien et al., 2012). We selected a histotype (MUC CRC) and analyzed the architecture of the human tumors in patients and of the tumors derived from cells transplanted into the mouse subcutaneous stroma. The histological assessment based on HES staining revealed two distinct architectures, PDX#1 and PDX#2 displayed tumor cell masses surrounded by mucin whereas PDX#3 showed tumors organized as sheets forming glandular structures delineating mucin areas (Fig. 2A, top panels; Fig. S1A). Of note, the phenotypes were more homogenous in the mice xenograft than in patients. We then assessed the apico-basolateral polarization of these tumors. PDX#3 harbored a conventional epithelial organization, with the apical membranes of cancer cells facing inward and delimiting a central lumen (apical-in phenotype). In contrast, the tumor cell clusters in PDX#1 and PDX#2 displayed an outward ezrin staining facing the mucin aureole, corresponding to the apical-out phenotype (Fig. 2A, bottom panels). Organoids have recently emerged as relevant experimental models to study oncogenesis (Dekkers et al., 2021). We generated tumor organoids from the three PDXs and embedded them in collagen-I gels as a surrogate for the peritumoral stroma (Ricard-Blum, 2011) to assess their organization and polarity. Strikingly, all organoids remained highly cohesive, and we never observed dissociation or single-cell detachment followed by invasion. We then assessed their polarity, either apical-in, apical-out or as partial phenotypes, by following their morphology (lumen and protrusions) and ezrin localization (Fig. S2). As with the patient TSIPs, although all organoids had an inverted apico-basolateral polarity in suspension (Fig. S1B,C), they adopted different topologies in collagen-I depending on the tumor they were originating from. Respectively, 84% and 98% of organoids produced from PDX#1 and PDX#2 displayed an apical-out topology in collagen-I (Fig. 2B,C). By contrast, organoids from PDX#3 harbored an apical-in phenotype and formed lumens in collagen-I (Fig. 2B,C). Electron microscopy confirmed the two polarity phenotypes observed by immunofluorescence, showing microvilli at internal (apical-in) or external (apical-out) membranes (Fig. 2D). Thus, the PDXs and the organoids recapitulate the observations made from the patients and attest that MUC CRCs represent a heterogenous group of cancers with different polarity orientation. The distinct topologies appeared *in vivo* in the murine

Journal of Cell Science (2022) 135, jcs259256. doi:10.1242/jcs.259256

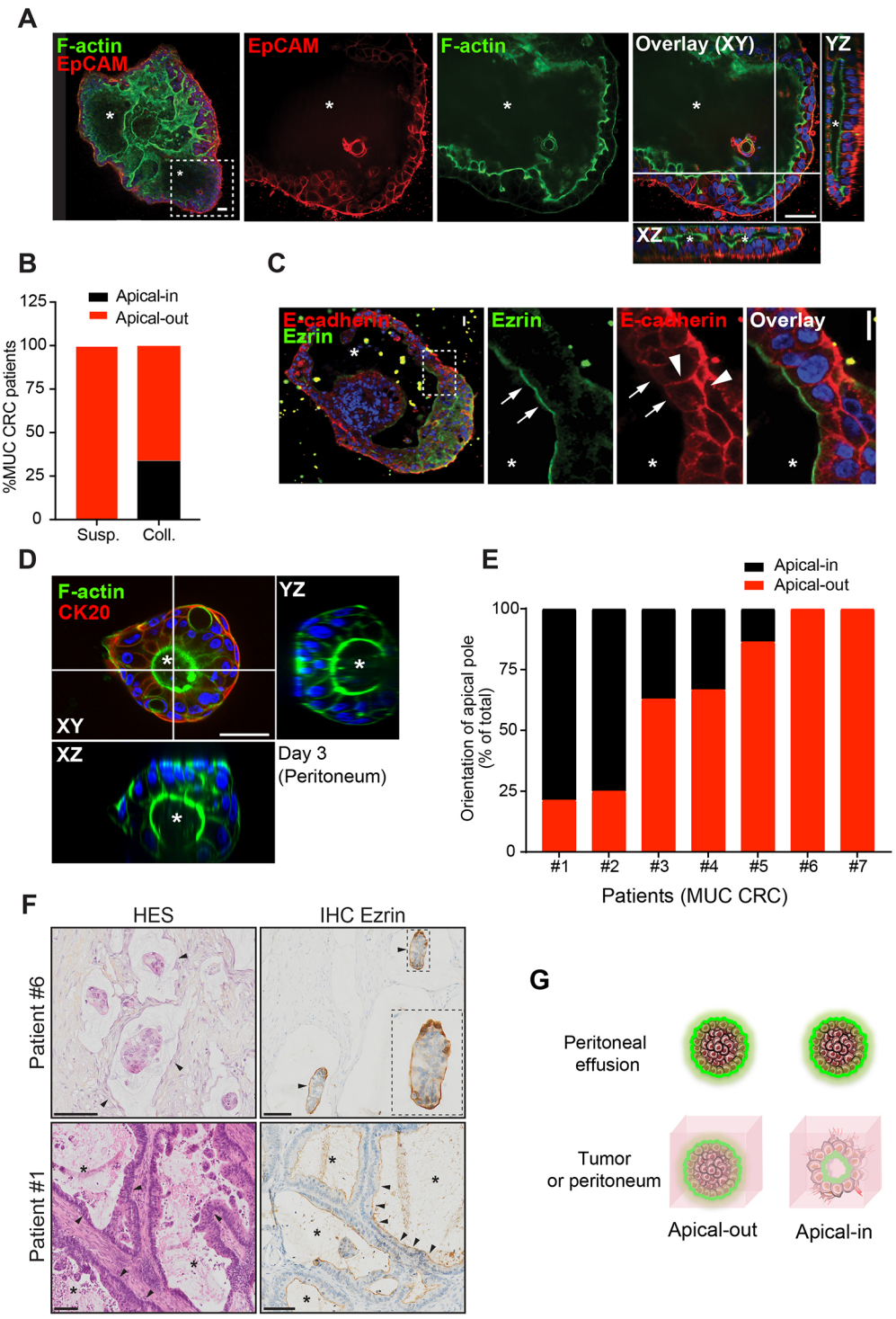

Fig. 1. MUC CRC patients display two distinct histological architectures and TSIP behaviors. (A) Representative images of a patient MUC CRC TSIP forming a luminal cavity after 6 days in a 3D collagen-I gel, immunostained for EpCAM, F-actin and DAPI (blue). *, luminal cavity. Scale bars: 50 µm. (B) Quantification of TSIPs polarity in suspension (from peritoneal effusions) and after 3 to 6 days in collagen-I gels. The graph shows the percentage of patients displaying apical-out vs apical-in organoids based on the outward or luminal localization of ezrin, respectively, in one confocal-Z-section (30 TSIPs/patient for 7 patients). (C) Representative image of a MUC CRC patient TSIP displaying and apical-in topology after spending 6 days in a collagen-I gel, immunostained for ezrin, E-cadherin and DAPI (blue). *, lumen; arrows, apical membrane enriched in ezrin; arrowheads, cell–cell junctions enriched in E-cadherin. Scale bars: 20 µm. (D) Representative images of a TSIP adhering to a peritoneal explant from the matching patient and forming a central cavity after 3 days, immunostained for CK20, F-actin and DAPI. *, luminal cavity. Scale bar: 50 µm. (E) Quantification of TSIP polarity gathered from peritoneal effusions after 6 days in collagen-I gels. The graph shows the percentage of apical-out versus apical-in TSIPs based on the outward or luminal localization of ezrin in one confocal-Z-section (30 TSIPs/patient for 7 patients). (F) HES staining and IHC for Ezrin of peritoneal metastases collected during cytoreductive surgery of MUC CRC patients #1 and #6. Images representative of seven patients. *, lumen; arrowheads, lining stroma (left), apical pole enriched in ezrin (right). Scale bars: 100 µm. (G) Schematic representation of TSIP polarity in suspension, in the primary tumor, in the peritoneum or after embedding in matrix. Data in B,E are represented as mean.

stroma and *in vitro* in simple collagen-I gels, showing this feature is mostly cell autonomous.

Apical-out and apical-in organoids harbor different expression profiles

We used the organoids to compare the expression profiles of the two topologies and determine the mechanism of polarity orientation in MUC CRCs. PDX#1, PDX#2 and PDX#3 organoids were maintained in suspension or embedded into collagen-I for 3 days, then, their RNA was extracted and analyzed (Fig. 3A, triplicates). Whole-transcriptome experiments were performed in each experimental condition for each PDX. Human Clarium S chip experiments were undertaken for each specimen, and, after robust multichip average (RMA) normalization, a supervised analysis was investigated by determining analysis of variance values. The response of the PDX organoids to collagen-I embedding was measured by using the significance analysis for microarray algorithm (Huber et al., 2015) for the transcriptome. These analyses revealed that collagen-I regulated more genes in organoids from PDX#3 (156 specific genes; Table S1) as compared to organoids from PDX#1 and PDX#2 (34 specific genes; Table S2), among which only two genes were in common (Fig. 3B). In line with these results, the global gene

Journal of Cell Science (2022) 135, jcs259256. doi:10.1242/jcs.259256

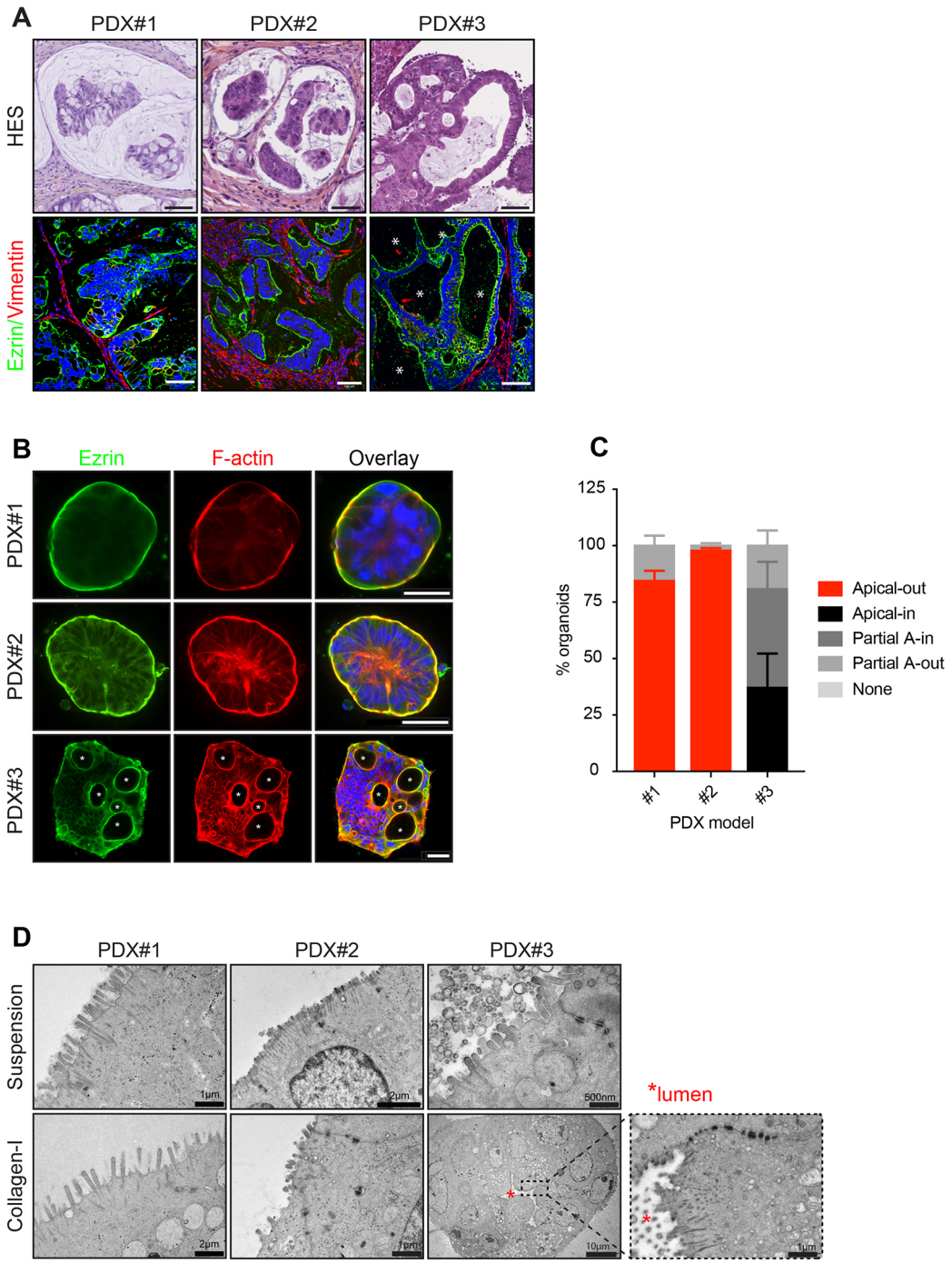

Fig. 2. Polarity orientation is a cell autonomous feature of MUC CRCs. (A) HES staining (top panel) and ezrin, vimentin (for stromal cells) and DAPI (blue) immunostaining (bottom panel) of MUC CRC PDX tumors: apical-out (PDX#1 and #2) and apical-in (PDX#3). *, lumens. Scale bars: 50 µm (top panel), 100 µm (bottom panel). (B) Organoids from PDXs after 3 days in collagen-I gels, immunostained for ezrin, F-actin and DAPI (blue). *, lumens. Scale bars: 50 µm. (C) Quantification of PDX organoid apico-basolateral polarity orientation based on criteria as shown in Fig. S2 in one confocal *Z*-section (n=3 independent experiments, with 85, 90 and 69 organoids counted for PDX#1, PDX#2 and PDX#3, respectively). (D) Electron microscopy images of organoids in suspension or after 3 days in 3D collagen-I gels showing microvilli at the periphery for PDX#1 and PDX#2 and at the lumen for PDX#3. Data in C are represented as mean±s.e.m. Images in A,D representative of three experiments.

signature of the collagen-I response allowed to drastically discriminate collagen-I-embedded PDX#3 organoids from all other transcriptomic profiles (Euclidean distances, Fig. 3C). This was confirmed to be significant by unsupervised principal component analysis (P-value=2.84×10^{-11}, Fig. 3D; Fig. S3). In order to identify the pathways differentially activated by collagen-I in organoids made from PDX#3 versus PDX#1 and PDX#2, we performed gene set enrichment analysis (GSEA; Subramanian et al., 2005). This revealed a repression of cell cycle progression and an activation of the Sonic hedgehog (SHH), transforming growth factor β (TGFβ), hypoxia and focal adhesion pathways with a respective normalized enrichment score (NES) of +2.07, +2.33, +2.67 and +1.47 (Fig. 3E, F). Overall, these analyses identified the signaling pathways activated by collagen-I in apical-in organoids (PDX#3) and reveals

Journal of Cell Science (2022) 135, jcs259256. doi:10.1242/jcs.259256

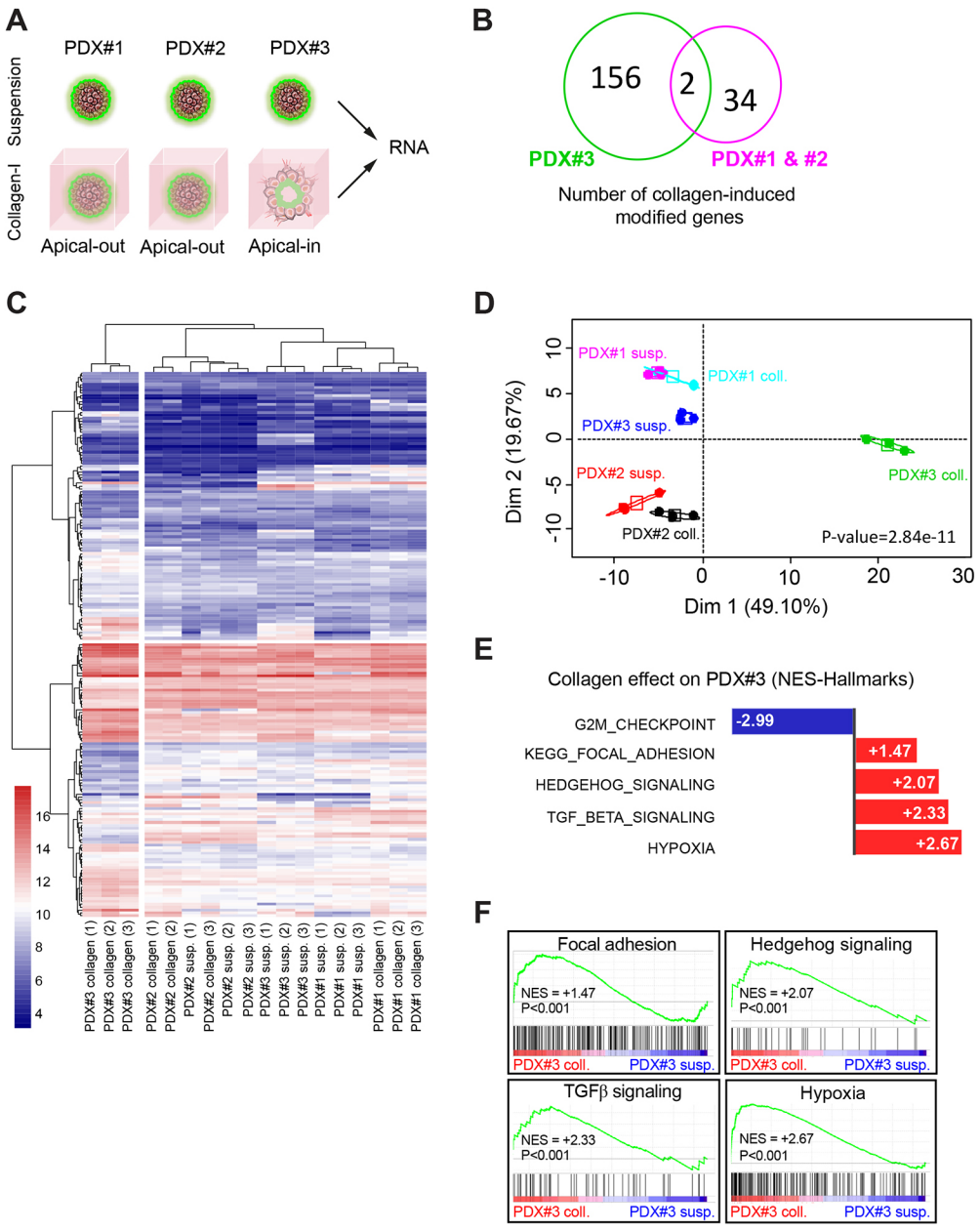

Fig. 3. Apical-in and apical-out organoids harbor different expression profiles when embedded into 3D collagen-I gels. (A) Schematic representation of the protocol used to generate mRNA for the microarray. Organoid RNA was extracted either after 3 days in suspension or after 3 days in 3D collagen-I gels. (B) Venn diagram representing the number of genes regulated by collagen-I embedding. (C) Discrimination of PDX#3 organoids in response to collagen-I stimulation. Results correspond to Table S1. (D) Results from B and C are confirmed by an unsupervised principal component analysis. (E,F) The GSEA revealed that PDX#3 organoids in collagen-I specifically repress the cell cycle progression (G2M checkpoint) and activate four pathways: focal adhesion, and Sonic hedgehog, TGFβ and hypoxia signaling. Data are represented as mean.

that they are not induced in apical-out CRC organoids (PDX#1 and #2) after embedding in ECM.

Downregulated TGFβ signaling prevents normal apico-basolateral polarity orientation in MUC CRC

To assess which one(s) of these signaling event(s) control(s) polarity orientation, we performed interference experiments using the organoids in collagen-I gels. No major components of the SHH pathway were differentially regulated between apical-in and apical-out tumors, and neither has this pathway been reported in the literature as regulating apico-basolateral polarity, thus, we did not investigate this pathway as a polarity regulator. To mimic hypoxia *ex vivo*, we incubated organoids from PDX#1 and PDX#2 with desferrioxamine (DFO), an inhibitor of HIF1α degradation. This treatment did not impact the polarity orientation relative to controls (Fig. S4A–C). Therefore, the hypoxic status of the cells is correlated to polarity but is not causative to its orientation.

We next investigated the participation of TGFβ signaling to polarity orientation. We first stimulated apical-out organoids made from PDX#1 and PDX#2 with TGFβ. We did not observe the induction of EMT and the dissociation of migratory single cells and therefore could assess the polarity of clusters. We observed a clear response of organoids from PDX#1 to TGFβ stimulation associated with an important decrease from 82% to 26% of inverted apical-out polarity (Fig. 4A,B). In contrast, the organoids from PDX#2 treated with TGFβ were indistinguishable from the controls, keeping their apical-out topology (Fig. 4A,B). Exome sequencing of TGFβ receptors and effectors identified that all three PDX models harbored the TGFBR2 K153fs frame-shift mutation reported to decrease TGFβ signaling (de Miranda et al., 2015), whereas only PDX#2 displayed a Smad4 W268* mutation, truncating half of the protein (Fig. 4C). This likely explains why this tumor is insensitive to TGFβ stimulation. Conversely, we inhibited TGFβ signaling in apical-in organoids generated from PDX#3 using two

Journal of Cell Science (2022) 135, jcs259256. doi:10.1242/jcs.259256

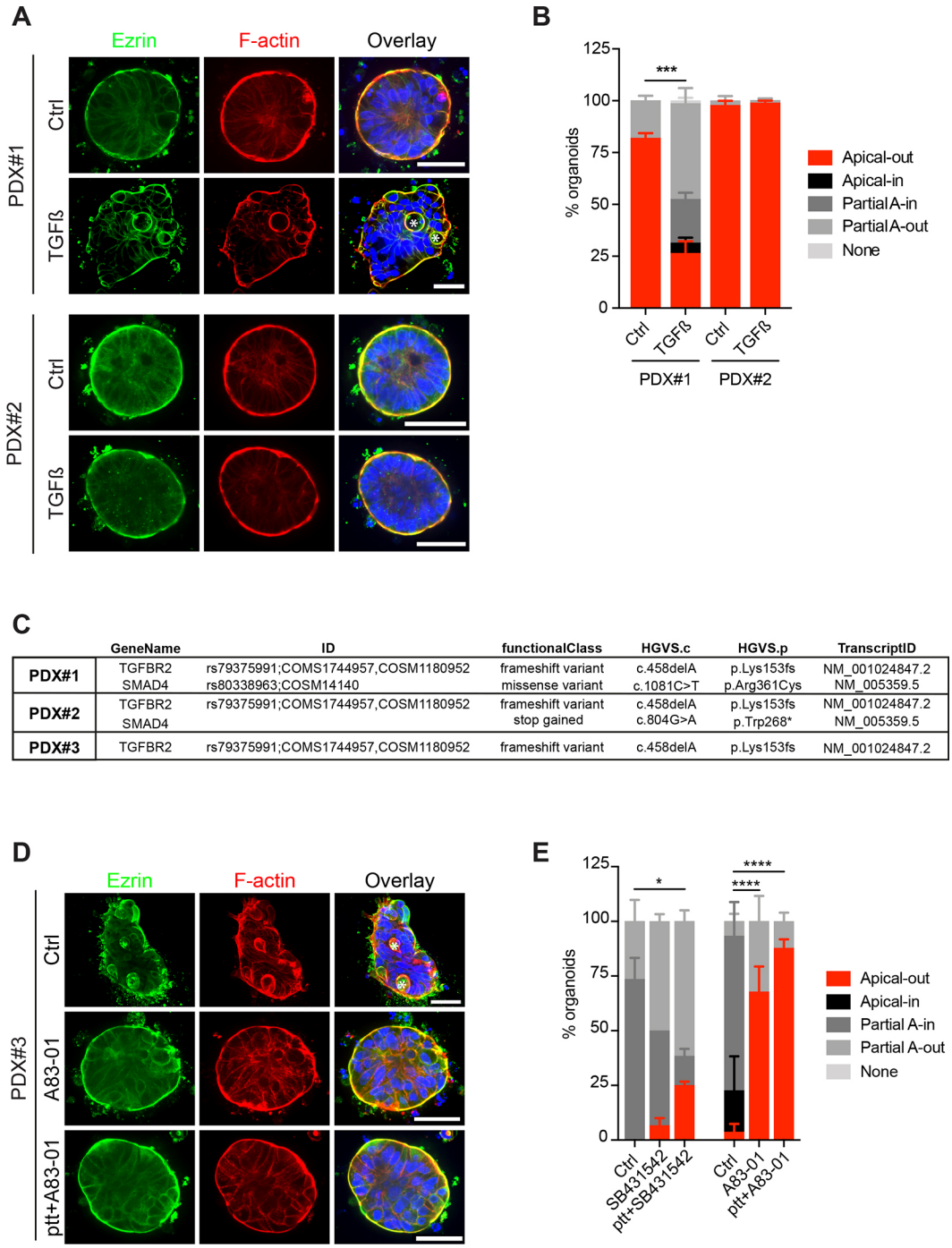

C

	GeneName	ID	functionalClass	HGVS.c	HGVS.p	TranscriptID
PDX#1	TGFBR2 SMAD4	rs79375991;COMS1744957,COSM1180952 rs80338963;COSM14140	frameshift variant missense variant	c.458delA c.1081C>T	p.Lys153fs p.Arg361Cys	NM_001024847.2 NM_005359.5
PDX#2	TGFBR2 SMAD4	rs79375991;COMS1744957,COSM1180952	frameshift variant stop gained	c.458delA c.804G>A	p.Lys153fs p.Trp268*	NM_001024847.2 NM_005359.5
PDX#3	TGFBR2	rs79375991;COMS1744957,COSM1180952	frameshift variant	c.458delA	p.Lys153fs	NM_001024847.2

Fig. 4. TGFβ is involved in the orientation of apico-basolateral polarity. (A) Immunostainings for ezrin, F-actin and DAPI (blue) after 3 days in collagen, in control condition or under treatment of TGFβ (20 ng/ml) for PDX#1 and #2. *, lumens. Scale bars: 50 µm. (B) Quantifications of PDX#1 and PDX#2 organoid phenotypes in collagen after TGFβ treatment (*n*=3 experiments for each PDX with 79 and 81 organoids counted for control and TGFβ conditions, respectively, for PDX#1, and 90 organoids counted for PDX#2 in both conditions). (C) Summary table recapitulating TGFβ signaling pathway mutations in PDXs, obtained by whole-exome sequencing. (D) Immunostainings for ezrin, F-actin and DAPI (blue) in control conditions, in PDX#3 pre-treated (ptt+A83-01) in suspension for 3 days or not, and then treated in collagen-I gels for 3 days with A83-01 (10 mM). *, lumen. Scale bars: 50 µm. (E) Quantification of PDX#3 organoid phenotypes treated and pre-treated with SB431542 (10 µM) or A83-01 (10 mM) (*n*=3 experiments with 82, 90 and 90 organoids counted for control, SB431542 and ptt+431542 conditions, respectively, and 61, 90 and 90 organoids counted for control, A83-01 and ptt+A83-01 conditions, respectively). ****P<0.0001, ***P<0.001, *P<0.05 (unpaired two-tailed *t*-tests were performed for B, one-way ANOVA with Tukey's post-hoc test for E). Data in B,E are represented as mean±s.e.m.

independent inhibitors of TGFβ receptor I (TGFBR1), SB431542 and A83-01. The drugs were either added to the collagen-I gels (treatment) or preceding their embedding in the matrix (pre-treatment). Both inhibitors altered polarity orientation in PDX#3 embedded into collagen-I (Fig. 4D and data not shown). Whereas the proportion of apical-in organoids dropped, the proportion with the apical-out phenotype increased significantly, from 0% to up to 26% and 88% after treatment showed that TGFβ signaling controls the apico-basolateral polarity orientation of MUC CRC organoids (Fig. 4E).

Journal of Cell Science (2022) 135, jcs259256. doi:10.1242/jcs.259256

The balance between integrin-mediated adhesion and contractility controls polarity orientation in MUC CRCs

The GSEA analysis also revealed that the focal adhesion pathway is activated in PDX#3 embedded in collagen-I, but not in the PDX#1 and PDX#2, which retained their apical-out topology in the matrix. Interestingly, integrin β1 (ITGB1), the main component of focal adhesions, controls the orientation of apico-basolateral polarity in normal renal cell lines through the downregulation of the ROCK serine/threonine kinases (Bryant et al., 2010, 2014; Ferrari et al., 2008; Liu et al., 2007). Thus, we tested whether ITGB1 and ROCK proteins could regulate polarity orientation in MUC CRC. Organoids from PDX#1 and PDX#2 were incubated with Y27632, a pharmacological inhibitor of ROCK proteins (Ishizaki et al., 2000). This treatment reduced the number of organoids with inverted polarity by 28- and 6-fold, respectively (Fig. 5A,B). Strikingly, this was associated with the appearance of internal apical membranes surrounding one or several luminal cavities, reminiscent of the apical-in topology (Fig. 5A,B). Conversely, inhibiting ITGB1 with the function-blocking antibody AIIB2 and shRNA (shITGB1) strongly repressed the apical-in phenotype in organoids from PDX#3, with the vast majority harboring an apical-out topology in collagen-I (87% and 52%, respectively; Fig. 5C,D). Using calyculin-A, an inhibitor of the phosphatase antagonizing ROCK-mediated myosin-II phosphorylation (Peterson et al., 2004), we observed a similar phenotype, with 90% of the organoids preserving their inverted apico-basolateral polarity (Fig. 5C,D). Thus, the topology of MUC CRCs is determined by the same core machinery as in non-transformed cells.

We then investigated whether the balance between adhesion and contractility could relate to defective TGFβ signaling. We hypothesized that decreased activation of non-canonical TGFβ signaling could increase the levels of RhoA and ROCKs, and therefore contractility. However, western blot experiments showed that the amount of phosphorylated myosin-II, a read-out for ROCK activity (Yu et al., 2005), was similar in the 3 PDXs (Fig. S5A). Thus, we reasoned that TGFβ inactivation could instead impair integrin function in apical-out organoids. We first observed that ITGB1 activity controls the apical-in orientation of organoids from PDX#1 and PDX#2 treated with Y27632 (Fig. S5B,C), indicating that β1 integrins are functional and do not harbor loss-of-function mutations in apical-out organoids. However, TGFβ is a known regulator of ITGB1 transcription (Margadant and Sonnenberg, 2010) and the microarray analysis revealed that PDX#1 and PDX#2 harbored lower levels of *ITGB1* mRNA (Fig. 5E). In line with this, we found that the levels of ITGB1 protein detected by immunofluorescence in PDX#1 and PDX#2 are lower than in PDX#3 and increased during polarity reversion in collagen-I gel (Fig. S5D,E). Finally, preventing ITGB1 activation using function blocking antibodies circumvented the apico-basolateral polarity reversion induced by TGFβ in PDX#1 (Fig. 5F,G). Together, these results show that the unbalanced levels of ITGB1-mediated adhesion and actomyosin contractility are involved in the inverted apical-out topology detected in MUC CRCs downstream of TGFβ signaling.

Apico-basolateral polarity orientation influences response to chemotherapies

In order to determine the physio-pathological relevance of MUC CRC apico-basolateral polarity orientation, we tested whether organoid topology could influence the response to chemotherapeutic agents. We compared the survival of PDX#1 and PDX#3 organoids, in their native or inverted topologies, after treatment with cytotoxic agents widely used in CRC – oxaliplatin, 5-fluorouracil (5-FU) and irinotecan (SN-38). We used the IC70 concentrations based on the dose–response curve obtained from a collection of 25 organoids derived from CRC patients (Fig. S6A). PDX#1 in its native topology (apical-out) and treated with Y27632 (apical-in, Fig. S6B) were incubated with the drugs for 2–5 days and the number of viable cells was assessed using ATP-bioluminescence (Fig. 6A). The viability of the organoids in response to the three drug treatments was increased in the apical-out topology, as shown by the apical-out/apical-in viability ratio, which is over 1 (Fig. 6A; Fig. S6C). Using a similar strategy, we added cytotoxic agents to PDX#3 in their native (apical-in) and inverted topologies (apical-out induced by AIIB2 function blocking antibody; Fig. S6B) topologies. Likewise, cell survival to the three drug treatments was enhanced in the apical-out as to compared with the apical-in topology (Fig. 6B; Fig. S6D). Together, these experiments on both PDX models ruled-out off-target effect from AIIB2 or Y27632. They pointed to the inverted apico-basolateral polarity as a protective topology against chemotherapeutic-induced cell death. This could be explained by the lower proliferation rate detected in the apical-out polarity (Fig. 6C,D). Furthermore, and independently of the genetic make-up of the tumor, we also observed lower mitotic indexes and proliferation rates in the live primary specimens harboring an apical-out topology as to compare with apical-in (Fig. 6E,F; presenting patient specimens included in Fig. 1).

Apico-basolateral polarity orientation correlates with patients' survival

Finally, to determine whether polarity orientation could impact the clinical outcome of patient with MUC CRCs, we performed a histological analysis using an independent published annotated cohort of MUC CRC patients (Barresi et al., 2015). The apico-basolateral polarity orientation of CRC clusters was automatically assessed using an algorithm created in Definiens Developer XD (Definiens, Munich, Germany) software and applied to 36 patient specimens. Tumor specimens were stained for CRC cell types (identified by cytokeratin 20 staining), stroma (Nuclear Red; pink) and the mucus (Alcian Blue; Fig. 7A, left panel). The polarity orientation was determined based on CRC cluster shapes and their relative localization to the stroma and the mucus. CRC clusters were classified into apical-in (red) or apical-out categories (yellow/green; Fig. 7A, right panels). The results obtained through this morphometry analysis showed that a third of patients (9/36) harbored mostly an apical-out organization and two-thirds (27/36) displayed a glandular apical-in architecture (Fig. 7B). We also calculated a polarity score, based on the ratio between apical-in and apical-out components. For the prediction of death from MUC CRC, we used receiver under operating characteristics (ROC) analyses (Zou et al., 2007) to calculate the most accurate cut-off values of the number of apical-out clusters and the polarity score. A log rank test with Kaplan–Meier curves showed that patients harboring a CRC with a high number of apical-out clusters (>92) had a significantly shorter cancer-specific survival (CSS) than patients having a CRC with a low count of apical-out clusters (≤92) (P=0.04; H.R., 2.5; c.i., 1–6.3) [H.R. is the hazard ratio, the ratio of the hazard rates corresponding to the conditions described by two levels of an explanatory variable (Cox, 1972)] (Fig. 7C). Similarly, the patients having a CRC with a low polarity score (ratio apical-in/apical-out <2.75) had significantly shorter CSS than those harboring a CRC with a high score (≥2.75) (P=0.02; H.R., 3.1; c.i., 1.1–8.4) (Fig. 7D). Together, these data point to two subgroups of MUC CRC patients based on the architecture of their tumor and

Journal of Cell Science (2022) 135, jcs259256. doi:10.1242/jcs.259256

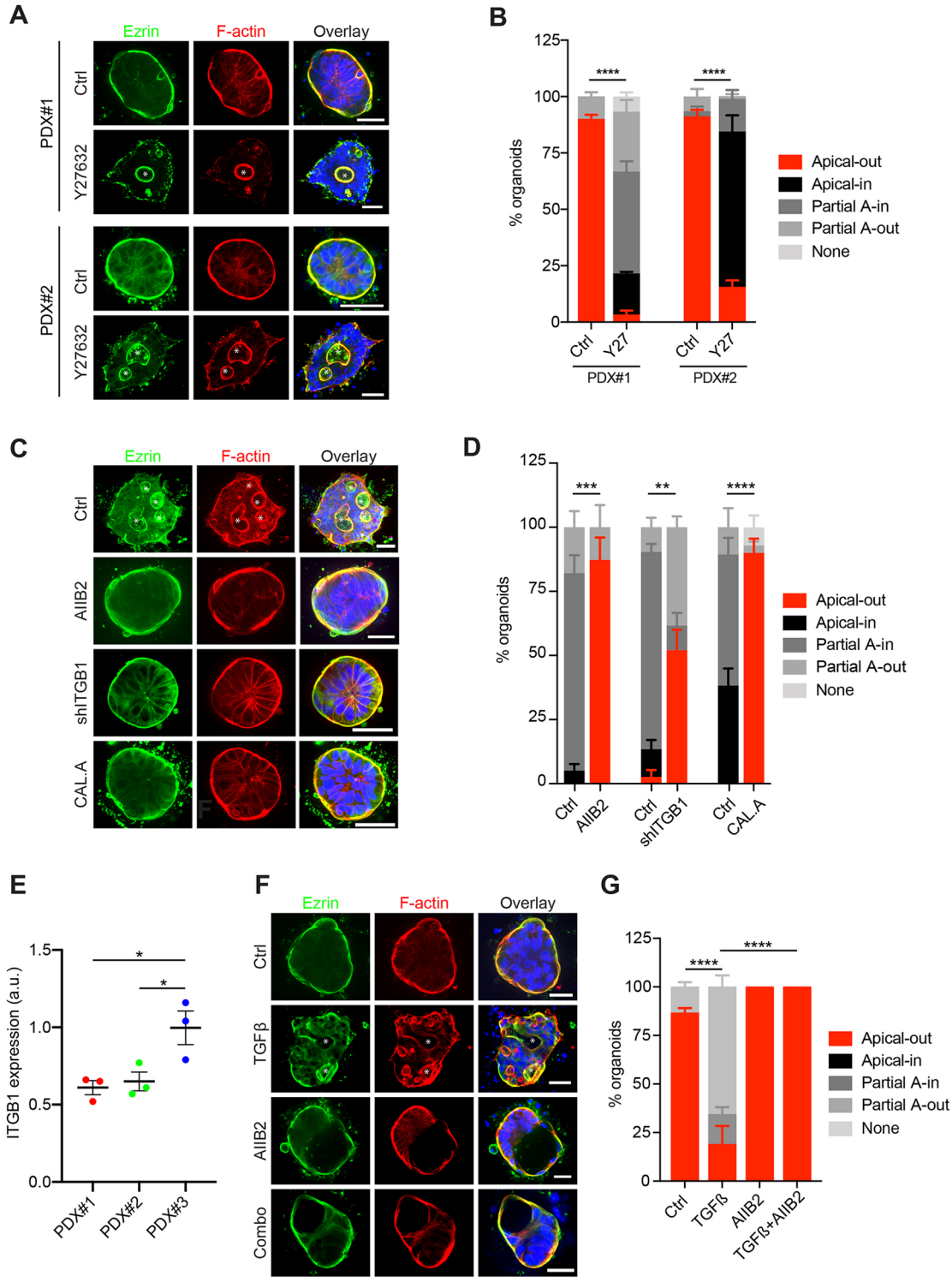

Fig. 5. The balance between adhesion and contractility drives organoids apico-basolateral polarity. (A) Organoids from PDX#1 (top panel) and PDX#2 (bottom panel) immunostained for ezrin, F-actin and DAPI (blue) after 6 days in collagen, in control condition or after treatment with Y27632 (25 µM). (B) Quantifications of PDX#1 and PDX#2 organoid phenotypes in collagen after Y27632 (Y27) treatment (n=3 experiments with 90 and 88 PDX1# organoids counted for control and Y27632 conditions, respectively, and 91 and 92 for PDX#2). (C) Organoids from PDX#3 after 3 days in collagen, in control condition or after treatment with AIIB2 (1 µg/ml), shITGB1 or calyculin-A (CAL.A, 1 nM) and immunostained for ezrin, F-actin and DAPI (blue). (D) Quantifications of PDX#3 organoid phenotypes in collagen after AIIB2, calyculin-A treatment or shITGB1 (n=3 experiments with 67 and 80 organoids counted for control and AIIB2 condition, respectively, 74 and 88 for control and shITGB1 conditions, respectively, and 75 and 69 for control and CAL.A, respectively). (E) *ITGB1* mRNA expression (from microarray analysis) of PDX#1, #2 and #3 after 3 days in collagen-I gels. (F) Organoids from PDX#1 immunostained for ezrin, F-actin and DAPI in control conditions and after treatment with TGFβ (20 ng/ml), AIIB2 (1 µg/ml) or the two combined in collagen-I gels. (G) Quantification of PDX#1 organoid phenotypes in collagen after TGFβ, AIIB2 or TGFβ and AIIB2 treatments (n=4 experiments with 120, 90, 116 and 120 organoids counted for control, TGFβ, AIIB2 and TGFβ+AIIB2 conditions, respectively). *, lumens. Scale bars: 50 µm. ****P<0.0001, ***P<0.001, **P<0.01, *P<0.05 (unpaired two-tailed t-tests were performed for B, D, E; one-way ANOVA with Tukey's post-hoc test for G). Data in B,D,E,G are represented as mean±s.e.m.

Journal of Cell Science (2022) 135, jcs259256. doi:10.1242/jcs.259256

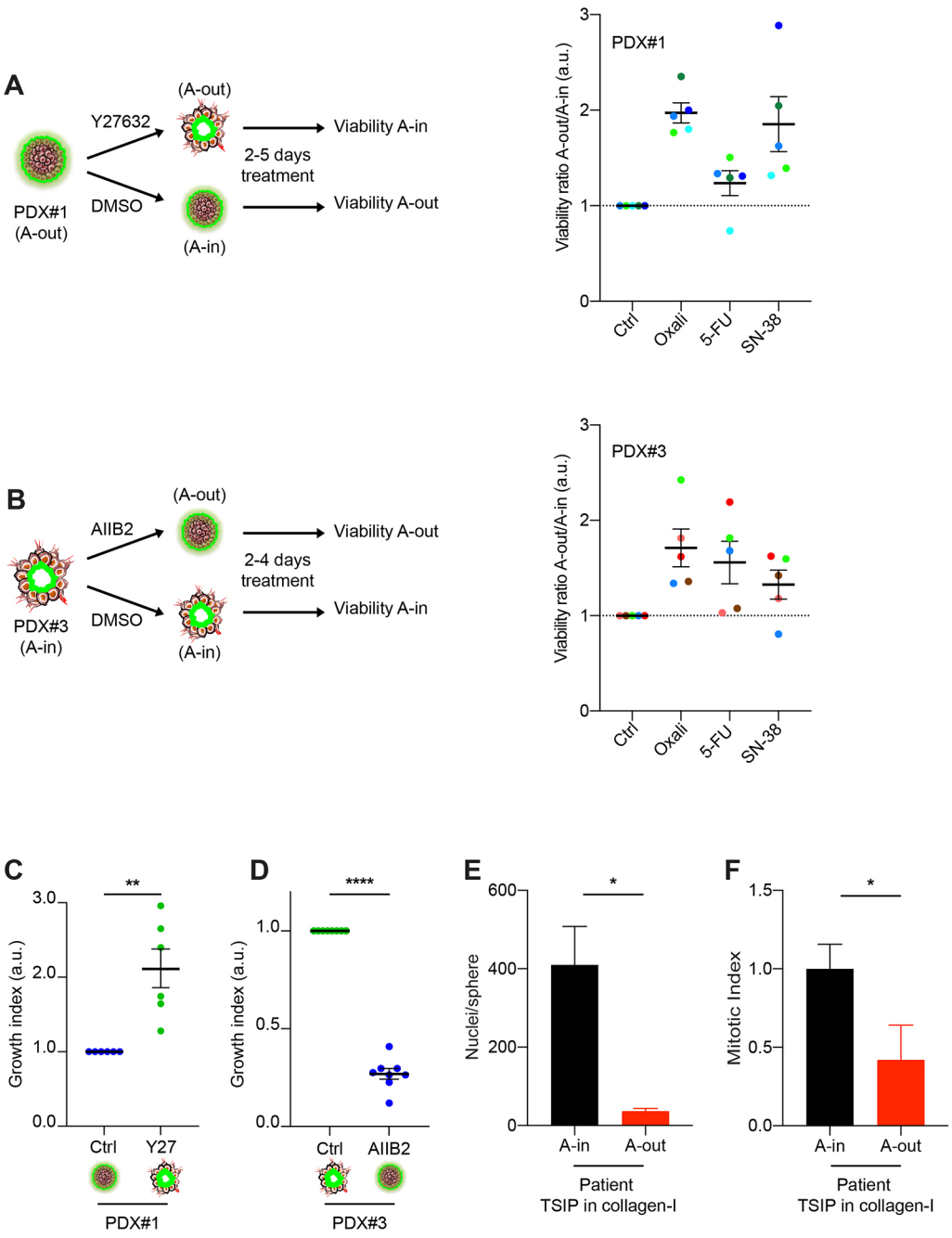

Fig. 6. Organoids apico-basolateral polarity could predict response to chemotherapy. (A) Left, schematic representation of the protocol for assessment of polarity-related chemosensitivity for PDX#1. Right, viability ratio A-out/A-in of PDX#1 organoids in control condition or after treatment for 2 to 5 days with oxaliplatin (Oxali, 10 µM), 5-fluorouracil (5-FU, 1.8 µM) or irinotecan (SN-38, 6.10^{-3} µM). (B) Left, schematic representation of the protocol for assessment of polarity-related chemosensitivity for PDX#3. Right, viability ratio A-out/A-in of PDX#3 organoids in control condition or after treatment for 2 to 4 days with oxaliplatin (Oxali, 10 µM), 5-fluorouracil (5-FU, 1.8 µM) or irinotecan (SN-38, 6.10^{-3} µM). Chemotherapeutic agents were used at the IC70 (see Fig. S5A). Each color point represents a separate experiment. Viability ratio calculation is detailed in Materials and Methods. (C) Growth index using ATP-bioluminescence for PDX#1 organoids in control condition (Ctrl) or after polarity reversion (Y27632), normalized to control condition. (D) Growth index using ATP-bioluminescence for PDX#3 organoids in control condition (Ctrl) or after polarity reversion (AIIB2), normalized to control condition. (E) Number of nuclei per TSIP, associated with apical-in and apical-out morphologies, counted using DAPI staining, respectively from n=19 TSIPs and 7792 nuclei and n=10 TSIPs and 364 nuclei from three patients. (F) Mitotic index, associated with apical-in and apical-out topologies, respectively from n=19 TSIPs and 7792 nuclei and n=10 TSIPs and 364 nuclei from three patients. ****P<0.0001, **P<0.01, *P<0.05 (unpaired two-tailed t-tests were performed for C,D,E and F). Data are represented as mean±s.e.m. a.u., arbitrary units.

the topology of the apico-basolateral polarity. The clinical outcome of the patients is correlated to polarity orientation with the apical-out MUC CRCs being associated with shorter cancer-specific survival.

DISCUSSION

Thus, the live and fixed primary cancer specimens retrieved from MUC CRC patients prove that apico-basolateral polarity is maintained in the course of their dissemination. However, apical-in and apical-out topologies exist, resulting from the cell-autonomous properties of the cancer and from the micro-environment, tissue or fluid that the clusters encounter in their journey to secondary sites. This study, together with several recent articles, clearly challenge the assumption that epithelial differentiation and polarity act as tumor suppressors (Negri et al., 2005; Saito et al., 2018). Here, we identified that MUC CRCs constitute a heterogenous histological group of cancers based on the apico-basolateral polarity orientation of the tumor. Most MUC CRCs originate from serrated precursor lesions, and as such they use a bona fide TSIP-based metastatic cascade where the apical-out phenotype is sustained at all stages, in tissues and fluids (Jass, 2007). In this study, we identified that about a third of the patients with MUC CRC produced TSIPs with inverted topology only transiently in peritoneal effusions, but had most of the tumor organized with a conventional apical-in glandular architecture in tissues. In this subset of patients, depending on the activation of integrins by ECM, the apico-basolateral polarity of the cancer clusters is switched ‘in’ and ‘out’ in the course of their dissemination.

The two distinct subgroups of MUC CRCs, based on their ability to switch polarity or to maintain a bona fide apical-out topology from the primary tumor to the metastatic site (TSIPs), could result

Journal of Cell Science (2022) 135, jcs259256. doi:10.1242/jcs.259256

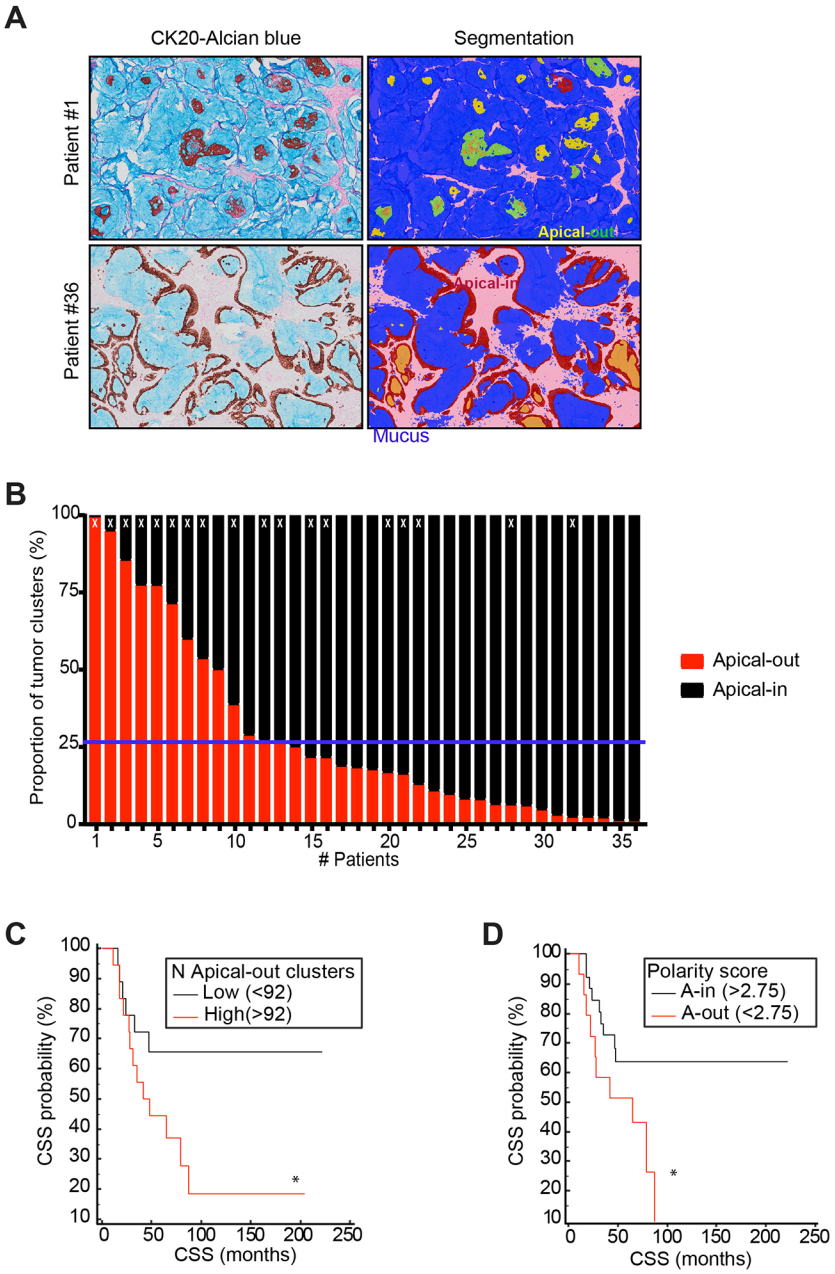

Fig. 7. Apico-basolateral polarity correlates with patients' survival. (A) Staining for CK20 and Alcian Blue for two MUC CRC patient samples and the corresponding segmentation from the morphometry analysis. The top panels show a region that is mostly represented by apical-out tumoral component (yellow and green), whereas the tumor in the bottom panels harbors an apical-in (red) architecture. (B) Quantitative representation of the apical-in (black) and apical-out (red) components for each MUC CRC patient (the white Xs represent patients with a number of apical-out clusters >92, used to generate the graph in C; the blue line indicates the polarity score to 2.75 used in the graph in D). (C,D) Kaplan–Meier curves displaying cancer-specific survival depending on the number of apical-out clusters (C) and polarity score (D). *P<0.05 (log-rank tests for C and D).

from divergent onco-morphogenetic pathways downstream of the serrated precursor lesion. Alternatively, this heterogeneity among MUC CRCs might result from the phenotypic convergence of distinct genetic groups of CRCs. Indeed, we previously identified an apical-in phenotype in conventional Lieberkuhnian CRCs (Libanje et al., 2019). Interestingly, pathologists have reported that radio-chemo therapies induce a mucin-secretory response in some of these cancers evolving toward MUC CRC in the course of the disease (Heino and Massagué, 1989; Thorpe et al., 2013).

Using transcriptomic analyses and interference experiments in organoids, we investigated the pathways regulating polarity orientation in MUC CRCs and identified integrin signaling as a crucial player in apico-basolateral polarity orientation. By interfering with ITGB1 signaling, we could switch the normal polarity of organoids from PDX#3 to an apical-out phenotype, demonstrating that ITGB1 is causative in this mechanism. This is in line with previous studies demonstrating that polarity orientation is dependent on integrin activation by their engagement with components of the ECM, such as laminin-1, collagen-IV and fibronectin (Gudjonsson et al., 2002; Okuyama et al., 2016). This also likely explains why in apical-in MUC CRCs the cancer cell clusters display an apical-out topology in suspension in peritoneal effusions where their integrins cannot be engaged and activated by ECM. Interestingly, this work revealed that a conserved intracellular core machinery controls the positioning of the apical pole away from the ECM in normal and transformed epithelial cells. This involves the balance between the adhesion and contractility, regulated by the GTPases Rac1 and RhoA through their effectors such as ROCKs (Bryant et al., 2010, 2014; Datta et al., 2017; Margaron et al., 2019 preprint).

We also showed that ITGB1 acts downstream of the TGFβ signaling – function-blocking antibodies against ITGB1 prevented the apical-in phenotype induced by TGFβ stimulation and low TGFβ signaling is associated with decreased ITGB1 mRNA levels.

Journal of Cell Science (2022) 135, jcs259256. doi:10.1242/jcs.259256

The canonical TGFβ signaling is known to regulate many cellular functions, including integrin-mediated adhesion, through the control of their dimerization, exposure at the cell surface or expression (Dongre and Weinberg, 2019; Gandalovičová et al., 2016; Sheppard et al., 1992; Zambruno et al., 1995). These results are also in line with our previous findings showing that TGFβ is an important regulator of polarity orientation (Zajac et al., 2018). Our experiments demonstrate that a downregulation in TGFβ prevents the organoids from correctly polarizing when embedded in matrix. In these MUC CRCs, this is dominated by the canonical effectors, as a truncation of Smad4 prevents polarity reversion in response to TGFβ stimulation. Although this pathway is mostly described to control apico-basolateral polarity establishment and maintenance (de Miranda et al., 2015; Gracia et al., 2019; Huang et al., 2020; Jung et al., 2019), we show that TGFβ also controls polarity orientation. This confirms our previous findings (Zajac et al., 2018) and observations made from 3D culture and micropatterned breast and kidney cell lines (Burute and Thery, 2012). Based on these studies, we envision MUC CRC carcinogenesis as, at least, a two-step process. First, early downregulation of TGFβ signaling promotes the budding of TSIPs from the serrated precursor lesion. Although this alteration is necessary for the polarity inversion, it is not sufficient. There is/are second alteration(s) that trigger(s) the robust apical-out phenotype observed in tissues for about two-thirds of patients. These alterations can either be within the TGFβ pathway itself (such as Smad4 loss of function mutation) or pathways that crosstalk with TGFβ, integrins and/or contractility.

Interestingly, although the TGFβ pathway is one of the main inducers of EMT, it is downregulated in MUC CRCs and other TSIP-producing tumors through a mutation in TGFBR2 that reduces the activation of its cytosolic effectors (Cheung et al., 2016; Zajac et al., 2018). This could likely explain why we never observe the dissociation of individual mesenchymal cell from patients explants or the three MUC CRC PDXs/organoids used in this study. This contrasts with single-cell dissociation and mesenchymal features associated with the invasion of a subset of organoids made from pancreatic cancer (Ashley et al., 2019). However, TSIP-based dissemination is associated with poor patient prognosis. This is in line with several studies on other EMT-independent modes of collective invasion, demonstrating that the interaction between cohesive tumor cells provides important signals for cancer cell survival in the peritumoral stroma or the hematogenous circulation (Aceto et al., 2014; Al Habyan et al., 2018; Padmanaban et al., 2019).

To test whether polarity orientation could be associated with different patient outcomes, we developed an automated morphometric tool and applied it to MUC CRC histological specimens to quantify a polarity score. Applied to the analysis of tumor specimens retrieved from a published cohort of patients with MUC CRC (Barresi et al., 2015), this revealed that the apical-out topology is associated with shorter patient survival. Functional investigation in patient-derived organoids showed that polarity orientation influences the response to chemotherapeutic treatment, with the apical-out topology being associated with increased drug resistance (Ashley et al., 2019). This could result from the low proliferative activity we detect in this subset of tumors, but alternative mechanisms might also be at play. Indeed, the apical and basolateral membranes are structurally and functionally very different (Gassama-Diagne et al., 2006; Kroepfl and Gardinier, 2001). Thus, the inverted topology, positioning the apical pole at the interface between cancer cells and their surrounding micro-environment, could also interfere with additional cellular functions and processes such as invasion, immune surveillance or drug intake or output (Kroepfl and Gardinier, 2001; Wosen et al., 2018). Intriguingly, the inverted apico-basolateral polarity of tumor cell clusters has been described in micropapillary histotypes of CRC, and breast, bladder, lung carcinomas, and is also associated with poor patient prognosis (Ahmed et al., 2012; Cserni, 2014; Kryvenko et al., 2013), showing this is a general feature of carcinomas. Thus, the polarity score could be used to stratify patients harboring a variety of cancers.

In this study, we developed innovative approaches and used organoids to bridge knowledge gained from histological and molecular profiling in order to decipher the mechanism of MUC CRCs organization and polarity. In the past decade, organoids have proven to be crucial tools for decryption of the biology of cancers, and they are currently being evaluated for their utility in the treatment of patients (Vlachogiannis et al., 2018; Yao et al., 2020). These cancer avatars have mainly been used to unlock the key mutational events associated with cell transformation or cancer progression and study the response and resistance to therapeutic agents (Drost and Clevers, 2018; Sato and Clevers, 2013; Tuveson and Clevers, 2019; Zanoni et al., 2020). Here, rather than cultivating organoids in Matrigel (components of the basal lamina) as usually done, we embedded them into collagen-I tridimensional hydrogels, an established surrogate of the peritumoral stroma (Doyle et al., 2015; Wolf and Friedl, 2011). This revealed that organoids recapitulate the main features of tumor architecture observed from patient histological specimens or primary explants, including the apico-basolateral polarity and its orientation. This is in agreement with parallel studies from our laboratory on ‘none otherwise specified’ (NOS) CRC and TSIPs (Libanje et al., 2019; Roy et al., 2017) as well as recent published work on pancreatic, breast cancer and glioblastomas (Goranci-Buzhala et al., 2020; Han et al., 2020; Koga et al., 2020; Padmanaban et al., 2020). Thus, organoids stand as tridimensional living tools that complement the inert histological 2D specimens, providing unique and relevant morpho-dynamic information on tumor cell behaviors.

MATERIALS AND METHODS

Recovery and characterization of peritoneal effusions from CRC patients

The human study protocols followed all relevant ethical regulations in accordance with the declaration of Helsinki principles. The study was approved by the ethics committee (CPP IDF 10), under protocol NI-2015-06-03, at Gustave Roussy and Lariboisière Hospitals. Written informed consent was obtained from all patients. Peritoneal effusions from a total of 59 patients with CRC were collected (as described in Zajac et al., 2018). In brief, the peritoneal effusions were collected immediately after laparotomy and before cytoreductive surgery. The fluid was collected by addition and reabsorption of 500 ml of saline solution and processed in the laboratory within 2 h after collection for characterization of polarity orientation.

Organoid preparation from patient-derived xenografts

Animal experiments were compliant with French legislation and EU Directive 2010/63. The project was validated by the Ethical Committee (CEEA) no. 26 and was then granted French government authorizations under number 517-2015042114005883 and 2734-2015111711418501. Mice were obtained from Charles River, housed and bred at the Gustave Roussy animal core facility (accreditation number E-94-076-11). Animals were humanely euthanized according to endpoints that were validated by the Ethical Committee and the French government (Ministère de l’Enseignement Supérieur, de la Recherche et de l’Innovation).

Three human colorectal tumors (PDX#1 corresponding to LRB-0009C, PDX#2 corresponding to IGR-0012P and PDX#3 corresponding to IGR-014P) from the CReMEC tumor collection were maintained in NSG mice

(NOD-scid IL2Rgamma^{null}, from Charles River, France) as previously described by Julien et al. (2012). Briefly, small tumor fragments were subcutaneously engrafted on the flank of anesthetized mice (2.5% isoflurane).

Tumor growth was measured at least once a week. When the volume reached 1500 mm^3, mice were killed and tumors were used for *ex vivo* experiments and 50 mm^3 fragments engrafted on the flank of new mice. Organoids were prepared according to Sato and Clevers (2013). and adapted for muco-secreting tumors as follows. The PDX#1, PDX#2 or PDX#3 tumors between 1000 and 1500 mm^3 were retrieved from the mice, minced into small fragments using a sterile scalpel and were incubated for 1 h at 37°C in a final volume of 5 to 10 ml of culture medium (Dulbecco's modified Eagle's medium; DMEM) without fetal bovine serum (FBS) and with 2 mg/ml collagenase (Sigma, C2139). The samples were then mixed with 20 ml of DMEM and filtered on 100 µm mesh size cell strainers (EASYstrainer, 542000). Digested tumor clusters were pelleted in by four pulse centrifugations at 277 ***g***. The tumor fragments, free of single cells, were maintained for 3 days in ultra-low attachment plates (Corning, CLS3471) in culture medium. Then, organoids were pelleted at 277 ***g*** and characterized [staining with apico-basolateral polarity markers demonstrated the organoids display the characteristics of TSIPs as show in Zajac et al. (2018)]. Organoids were used for survival and invasion experiments as well as for mice intraperitoneal injection.

Western blotting

Cells were lysed with SDS sample buffer (62.5 mM Tris-HCl pH 6.8, 10% glycerol, 0.002% Bromophenol Blue, 2% SDS, and 5% β-mercaptoethanol) and lysates were boiled for 10 min. The samples were subjected to SDS-PAGE and proteins were transferred to nitrocellulose membranes (GE Healthcare). Membranes were incubated for 30 min in Blocking Solution [Tris-buffered saline (TBS) containing 0.1% Tween-20 and 3% bovine serum albumin (BSA)] and further incubated with the appropriate primary antibody overnight at 4°C. Primary antibodies against the following proteins were used at the indicated dilutions: phospho-T18/S19-MLC (1:1000, Cell Signaling Technology, 3674S), MLC2 (1:1000, Cell Signaling Technology, 3672S) and HSC70 (1:4000, Santa Cruz Biotechnology, sc-7298). The membranes were then washed three times with 0.1% Tween-20 in TBS and incubated for 45 min with secondary antibody conjugated to horseradish peroxidase (GE Healthcare). Bound antibodies were detected with enhanced chemoluminescence.

ITGB1 silencing using shRNA

10^4 clusters from PDXs obtained right after tumor dissociation (see method above) were placed in 1 ml of DMEM in a low-attachment six-well plate, and were infected using the lentiviral vectors shITGB1 (VB200629-1112fft, Vector Builder) or the control (pRRL.TRE3GDsRed; Fellmann et al., 2013) based on the multiplicity of infection (MOI) given by the manufacturer or shRNA *Renilla* for the control condition. The following day, 2 ml of medium were added. After 3 days, the organoids were placed in collagen-I gels (see method below) and the infection rate was observed using GFP. An organoid was considered properly infected and expressing the shRNA if at least 80% of the cells were GFP positive.

Organoid polarity assessment

Collagen-I (Corning, 354236) was neutralized with 1.0 M NaOH and 10× MEM (Life Technologies, 21430-02) according to the ratio: 1.0:0.032:0.1 (v/v/v). The concentration was then adjusted to 2 mg/ml with 1× DMEM, and the collagen-I was incubated on ice for 1–1.25 h. The organoids embedded in neutralized collagen-I were added on top of the pre-coated well at a concentration of 30–50 organoids/5 µl (ibidi 8-well chamber). The gel was allowed to polymerize for 45 min at 37°C. Organoids were then cultured in culture medium supplemented with FBS 10% for up to 6 days (3 days for PDX#3). The drugs were diluted in the medium as follows: AIIB2 (DSHB, AB528306), A83-01 (Sigma-Aldrich, 909910-43-6, 100 µM), blebbistatin (Calbiochem, 203391, 10 µM), calyculin-A (Clinisciences, sc-24000A, 1 nM), SB431542 (Sellekchem, S1067, 10 µM), TGFβ (R&D System, P01137, 20 ng/ml) and Y27632 (Calbiochem, 688000, 25 µM).

After incubation for 3 to 6 days in low-adherence culture plates, the apico-basolateral polarity of organoids was quantified after immunostaining using anti-ezrin (1:1000, CPTC-Ezrin-1, DSHB) or anti-p-ERM antibodies (1:1000, #3141 Cell Signaling). Organoids are considered to have an inverted polarity when at least 75% of the total peripheral cells display an outward apical pole in one confocal *Z*-section and displays protrusions (see Fig. S2 for phenotypes).

For organoids stained in suspension, they were fixed 10 min in 4% paraformaldehyde (PFA) after 3 days in low adherence culture plates in complete medium then embedded in collagen-I gels for immunofluorescent staining.

Immunofluorescence, antibodies, histology and immunohistochemistry

Immunofluorescence

Samples were washed twice in PBS supplemented with Ca^{2+} (0.1 mM) and Mg^{2+} (1 mM) and fixed in 4% PFA for 45 min (TSIPs and peritoneum). Permeabilization was performed in PBS supplemented with 0.5% Triton X-100 for 45 min. Primary antibodies were incubated overnight at 4°C at the dilutions listed below in antibody diluent, PBS with 10% serum supplemented by 0.1% Triton X-100. Secondary antibodies used at 1:500 [Jackson ImmunoResearch, AffiniPure goat anti-mouse-IgG conjugated to Alexa Fluor 488 (715-545-150), AffiniPure goat anti-rabbit-IgG conjugated to Cy3 (711-165-152) or Life Technologies goat anti-mouse-IgG conjugated to Alexa Fluor 647, A21241, donkey anti-rabbit-IgG conjugated to Alexa Fluor 488, A21206)], phalloidin, 1:1000 (Life Technologies) and DAPI (1 µg/ml) were incubated overnight at 4°C or 2 h at room temperature.

Primary antibodies

Primary antibodies used were against: cytokeratin 20 (CK20; 1:200, Abcam, ab76126), E-cadherin (1:200, Abcam, ab1416), EpCam (1:200, MA5-12436), ezrin (1:100, DSHB, AB_210031), GM130 (1:200, NovusBio, NBP1-89757) and vimentin (1:500, ThermoFisher Scientific, PA1-16759).

Histology

CRC and peritoneum specimens obtained after surgical resection were formalin fixed and paraffin embedded according to routine protocols. Peritoneal effusions were concentrated by centrifugation (277 ***g*** for 15 min) and fixed in formalin, then embedded for cytoblock. Sections (3 µm) of formalin-fixed and paraffin-embedded samples were deparaffinized, unmasked (pH 8) and rehydrated before HES or Alcian Blue staining, immunohistochemistry or immunofluorescence.

Immunohistochemistry

Sections were immunostained for ezrin (1:100; 610603, BD Biosciences) or with anti-CK20 mouse monoclonal antibody (clone Ks20.8, Dako). Stainings were performed with Ventana BenchMark XT immunostainer (Ventana Medical Systems) using the UltraView DABv3 kit (Ventana). The chromogene was 3,3′-diaminobenzidine (DAB) in all the stainings. Histochemical staining with Alcian Blue (pH 2.5) was performed with Ventana BenchMark Special Stains (Ventana Medical Systems) utilizing the V1.00.0010 process. Peritoneal effusion smears were stained using May–Grünwald–Giemsa stain.

Automated morphometry analysis

Image analysis was performed after manual selection of the regions of interest by the senior pathologist. As these regions were too large to be assessed in totality, they were divided into blocks of pixels that were processed individually and finally stitched. Images show four different classes: background, DAB-stained cytokeratin (CK), Alcian Blue-colored mucus areas and nuclear red (pink) colored areas of stroma. All these classes were first segmented. Background areas are pixels whose brightness is higher than 215. CK clusters are pixels whose value is lower than 165 on the blue component image. Mucin areas are pixels whose red component on blue component ratio is lower than 1, whereas stroma areas are pixels whose red on blue ratio is higher than 1, but that are not CK. Connected components are then computed for each class and small areas are discarded. To find the apical status of each CK cluster, the program

(QuPath; https://qupath.readthedocs.io/) identifies the position CK clusters, mucin and stroma areas, defined as mentioned above, and then detemines if it is surrounded by mucus (apical-out) or if it touches or is enclosed by a stroma area (apical-in). CK clusters surrounded by mucus that enclose a mucus area are discarded.

Microscopy, images treatment and analyses

Confocal imaging

Images were acquired using a SpinningDisk CSU-W1 microscope (Yokogawa) with a ZylasCMOC camera piloted with an Olympus X83. Images were processed using ImageJ or Metamorph software.

Electron microscopy

Isolated TSIPs were fixed in 2% glutaraldehyde in 0.1 M phosphate buffer pH 7.3 and deposited in drops of neutralized collagen-I (2 mg/ml) and allowed to polymerize for 10 min at room temperature laid on a glass coverslip. TSIPs were washed 30 min in phosphate buffer, post-fixed with 2% osmic acid at room temperature and rinsed in water. Samples were dehydrated in ethanol and embedded in Epon. Polymerization was complete after 48 h at 60°C. Ultrathin sections were collected on 100-mesh grids coated with Formvar and carbon, stained with uranyl acetate and lead citrate and observed with a FEI Technai Spirit transmission electron microscope at 80 Kv. Digital images were taken with a SIS MegaviewIII CCD camera.

Microarray

Samples preparation

RNA was extracted using the RNeasy minikit (Qiagen, Cat. No. 74104) from organoids either after 3 days in suspension (wash one time in PBS supplemented with Ca^{2+} and Mg^{2+} as mentioned above) or after 3 days in collagen-I gels (2 mg/ml, see Organoid polarity assessment section).

Transcriptome experiments

Whole-transcriptome experiments have been processed on each PDX line: 009C (#1), 012P (#2) and 014P (#3) and two experimental conditions: culture in suspension and culture on collagen. Each biological condition was tested in triplicate inside the transcriptome experimental map, which represents 18 transcriptome experiments. Starting from 100 ng of total RNA microarray, probes were synthetized and labeled with WT Plus Affymetrix chemistry in order to hybridized Clarium S Human microarray chip in Affymetrix microarray station.

Transcriptome analysis

Transcriptome analysis was performed with RMA normalization algorithm from Transcriptome Analysis Console (TAC, Applied Biosystems) software version 4.0. Two-way analysis of variance (ANOVA) was performed with MEV standalone software (version 4.9.0) with implementation of 500 permutations and decomposition on supervised factors: collagen-I effect, PDX phenotype IN & OUT. During this supervised analysis, the interaction factor was subtracted from the results.

Downstream bioinformatics analyses were performed with the open-source R software environment version 3.5.3 under Bioconductor dependencies (Huber et al., 2015). Supervised differential expressed gene signature to see collagen-I effect on PDX was performed with Significance Analysis for Microarray (SAM) algorithm (Tusher et al., 2001) with a fold change threshold of 2 and a false discovery rate (FDR) less than 5%. Expression heatmaps were drawn with pheatmap R-package with transcriptome normalized data. Unsupervised principal component analysis representation used the FactoMineR library. Geneset enrichment analysis was undertaken with Java standalone software GSEA version 4.0.3 (Subramanian et al., 2005). The microarray data are available on GEO with the access number GSE152299.

Assessment of polarity-related chemosensitivity

Organoids were prepared as described above (see Organoid preparation from PDXs section). After 3 days in suspension, they were filtered on a 70 µm cell strainer and placed in a collagen-I mix (see Organoid polarity assessment section) and evenly distributed in a 48-wells NUNC plate (ThermoFisher, #150687) using the Integra Assist Plus. Polarity reversion was obtained by incubating with Y27632 or AIIB2 on PDX#1 and PDX#3 respectively (see Organoid polarity assessment section).

After polarity reversion was achieved, the medium was withdrawn and drugs were added using the Tecan D300e (software: D300e control version3.4.1) as follows: 5-fluorouracil, oxaliplatin and irinotecan at the IC70 determined on CRC organoids. Control conditions were obtained using DMSO. After 2 days, ATP levels were assessed using CellTiter-Glo 3D according to the manufacturer's instructions, and bioluminescence was measured with the BioTek Synergy LK (software: Gen5™ version 3.10) in white-bottom 96-well plates.

The ATP bioluminescence signal was averaged over the three wells of the same condition in the apical-in or apical-out topology. This provided ATP (Chemo A-in) or ATP (Chemo A-out) values when organoids were treated with a chemotherapeutic agent, and ATP (Ctrl A-in) or ATP (Ctrl A-out) in control condition.

Viability in apical-in and apical-out topologies were then calculated as follows:

$$\text{Viability A-in} = \frac{\text{ATP(Chemo A-in)}}{\text{ATP(CtrlA-in)}} \quad \text{and}$$

$$\text{Viability A-out} = \frac{\text{ATP(Chemo A-out)}}{\text{ATP(Ctrl A-out)}}.$$

Finally, the ratio between apical-in and apical-out topologies was calculated as:

$$\text{Viability ratio} = \frac{\text{Viability A-out}}{\text{Viability A-in}}$$

Acknowledgements

We thank all the patients who participated in this study and the medical staff for their assistance with the acquisition of primary human specimens. We thank the members of the Jaulin Lab and the Digestive Cancer Unit for discussion, technical services provided by PFIC and PETRA core facilities (especially O. Bawa and V. Marty). We thank DSHB (University of Iowa) for antibodies. Results in this article (except Fig. 6, Fig. S1A, Fig. S5E and Fig. S6) are reproducted from the PhD thesis of Charlotte Canet-Jourdan (Paris-Saclay University, 2021).

Competing interests

The authors declare no competing or financial interests.

Author contributions

Conceptualization: C.C.-J., D.-L.P., C.N.-V., J.C., O.Z., C.D., P.G., M.D., F.J.; Methodology: C.C.-J., D.-L.P., C.N.-V., O.Z., J.-B.L., E.G.-M., N.S., J.A., J.R., M.P., S.S., G.P., P.D., V.B., F.J.; Software: C.C.-J., O.Z., C.D., N.S., J.A., S.S., V.B.; Validation: C.C.-J., D.-L.P., C.N.-V., J.C., O.Z., C.D., F.J.; Formal analysis: C.C.-J., D.-L.P., C.N.-V., J.C., O.Z., C.D., J.-B.L., E.G.-M., N.S., J.R., S.S., G.P., V.B.; Investigation: C.C.-J., D.-L.P., C.N.-V., O.Z., V.B.; Resources: C.C.-J., D.-L.P., C.N.-V., J.C., O.Z., G.P., M.G., P.D., M.D., V.B., F.J.; Data curation: C.C.-J., C.N.-V., J.C., O.Z., J.-B.L., E.G.-M., J.R., M.P., J.R.R.M.; Writing - original draft: J.C., F.J.; Writing - review & editing: C.C.-J., D.-L.P., C.D., J.R.R.M., F.J.; Visualization: C.C.-J., O.Z., C.D., N.S., J.A., J.R.R.M., P.D., F.J.; Supervision: F.J.; Project administration: F.J.; Funding acquisition: F.J.

Funding

This work was supported by the Institut National Du Cancer INCA-PLBIO program (2018-1-PL BIO-04-1, 2020-1-PL BIO-04), Agence Nationale de la Recherche (ANR-20-CE13-0031-01), Institut National de la Santé et de la Recherche Médicale (INSERM) programme 3R (20CR046-00), La Ligue Contre le Cancer (comité 94), subvention foundation ARC (PAJ20181208275), the Gustave Roussy Foundation ("Mars Bleu" and parrainage), doctoral scholarship from Paris-Saclay University and the French Ministry of Superior Education, la Fondation Pour la Recherche Médicale (FDT201904007976) and Research and the 'taxe d'apprentissage' Gustave Roussy (2016 to C.C.-J.).

Data availability

The microarray data are available on GEO with the accession number GSE152299.

Peer review history
The peer review history is available online at https://journals.biologists.com/jcs/article-lookup/doi/10.1242/jcs.259256.

References

Aceto, N., Bardia, A., Miyamoto, D. T., Donaldson, M. C., Wittner, B. S., Spencer, J. A., Yu, M., Pely, A., Engstrom, A., Zhu, H. et al. (2014). Circulating tumor cell clusters are oligoclonal precursors of breast cancer metastasis. *Cell* **158**, 1110-1122. doi:10.1016/j.cell.2014.07.013

Ahmed, A. R. H., Griffiths, A. B., Tilby, M. T., Westley, B. R. and May, F. E. B. (2012). TFF3 is a normal breast epithelial protein and is associated with differentiated phenotype in early breast cancer but predisposes to invasion and metastasis in advanced disease. *Am. J. Pathol.* **180**, 904-916. doi:10.1016/j.ajpath.2011.11.022

Al Habyan, S., Kalos, C., Szymborski, J. and McCaffrey, L. (2018). Multicellular detachment generates metastatic spheroids during intra-abdominal dissemination in epithelial ovarian cancer. *Oncogene* **37**, 5127-5135. doi:10.1038/s41388-018-0317-x

Ashley, N., Ouaret, D. and Bodmer, W. F. (2019). Cellular polarity modulates drug resistance in primary colorectal cancers via orientation of the multidrug resistance protein ABCB1. *J. Pathol.* **247**, 293-304. doi:10.1002/path.5179

Barresi, V., Reggiani Bonetti, L., Ieni, A., Domati, F. and Tuccari, G. (2015). Prognostic significance of grading based on the counting of poorly differentiated clusters in colorectal mucinous adenocarcinoma. *Hum. Pathol.* **46**, 1722-1729. doi:10.1016/j.humpath.2015.07.013

Bilder, D. (2004). Epithelial polarity and proliferation control: links from the Drosophila neoplastic tumor suppressors. *Genes Dev.* **18**, 1909-1925. doi:10.1101/gad.1211604

Bilder, D., Li, M. and Perrimon, N. (2000). Cooperative regulation of cell polarity and growth by *Drosophila* tumor suppressors. *Science* **289**, 113-116. doi:10.1126/science.289.5476.113

Brabletz, T., Hlubek, F., Spaderna, S., Schmalhofer, O., Hiendlmeyer, E., Jung, A. and Kirchner, T. (2005). Invasion and metastasis in colorectal cancer: epithelial-mesenchymal transition, mesenchymal-epithelial transition, stem cells and β-catenin. *Cells Tissues Organs* **179**, 56-65. doi:10.1159/000084509

Bryant, D. M., Datta, A., Rodríguez-Fraticelli, A. E., Peränen, J., Martín-Belmonte, F. and Mostov, K. E. (2010). A molecular network for de novo generation of the apical surface and lumen. *Nat. Cell Biol.* **12**, 1035-1045. doi:10.1038/ncb2106

Bryant, D. M., Roignot, J., Datta, A., Overeem, A. W., Kim, M., Yu, W., Peng, X., Eastburn, D. J., Ewald, A. J., Werb, Z. et al. (2014). A molecular switch for the orientation of epithelial cell polarization. *Dev. Cell* **31**, 171-187. doi:10.1016/j.devcel.2014.08.027

Burute, M. and Thery, M. (2012). Spatial segregation between cell–cell and cell–matrix adhesions. *Curr. Opin. Cell Biol.* **24**, 628-636. doi:10.1016/j.ceb.2012.07.003

Cheung, K. J., Gabrielson, E., Werb, Z. and Ewald, A. J. (2013). Collective invasion in breast cancer requires a conserved basal epithelial program. *Cell* **155**, 1639-1651. doi:10.1016/j.cell.2013.11.029

Cheung, K. J., Padmanaban, V., Silvestri, V., Schipper, K., Cohen, J. D., Fairchild, A. N., Gorin, M. A., Verdone, J. E., Pienta, K. J., Bader, J. S. et al. (2016). Polyclonal breast cancer metastases arise from collective dissemination of keratin 14-expressing tumor cell clusters. *Proc. Natl. Acad. Sci. USA* **113**, E854-E863. doi:10.1073/pnas.1508541113

Commander, R., Wei, C., Sharma, A., Mouw, J. K., Burton, L. J., Summerbell, E., Mahboubi, D., Peterson, R. J., Konen, J., Zhou, W. et al. (2020). Subpopulation targeting of pyruvate dehydrogenase and GLUT1 decouples metabolic heterogeneity during collective cancer cell invasion. *Nat. Commun.* **11**, 1533. doi:10.1038/s41467-020-15219-7

Cox, D. R. (1972). Regression models and life-tables. *J. R. Stat. Soc. Series B Stat. Methodol.* **34**, 187-220. http://www.jstor.org/stable/2985181

Cserni, G. (2014). Reversed polarity of the glandular epithelial cells in micropapillary carcinoma of the large intestine and the EMA/MUC1 immunostain. *Pathology* **46**, 527-532. doi:10.1097/PAT.0000000000000144

Datta, A., Sandilands, E., Mostov, K. E. and Bryant, D. M. (2017). Fibroblast-derived HGF drives acinar lung cancer cell polarization through integrin-dependent RhoA-ROCK1 inhibition. *Cell. Signal.* **40**, 91-98. doi:10.1016/j.cellsig.2017.09.001

de Miranda, N. F. C. C., van Dinther, M., van den Akker, B. E. W. M., van Wezel, T., ten Dijke, P. and Morreau, H. (2015). Transforming growth factor β signaling in colorectal cancer cells with microsatellite instability despite biallelic mutations in TGFBR2. *Gastroenterology* **148**, 1427-1437.e8. doi:10.1053/j.gastro.2015.02.052

Dekkers, J. F., van Vliet, E. J., Sachs, N., Rosenbluth, J. M., Kopper, O., Rebel, H. G., Wehrens, E. J., Piani, C., Visvader, J. E., Verissimo, C. S. et al. (2021). Long-term culture, genetic manipulation and xenotransplantation of human normal and breast cancer organoids. *Nat. Protoc.* **16**, 1936-1965. doi:10.1038/s41596-020-00474-1

Dongre, A. and Weinberg, R. A. (2019). New insights into the mechanisms of epithelial-mesenchymal transition and implications for cancer. *Nat. Rev. Mol. Cell Biol.* **20**, 69-84. doi:10.1038/s41580-018-0080-4

Doyle, A. D., Carvajal, N., Jin, A., Matsumoto, K. and Yamada, K. M. (2015). Local 3D matrix microenvironment regulates cell migration through spatiotemporal dynamics of contractility-dependent adhesions. *Nat. Commun.* **6**, 8720. doi:10.1038/ncomms9720

Drost, J. and Clevers, H. (2018). Organoids in cancer research. *Nat. Rev. Cancer* **18**, 407-418. doi:10.1038/s41568-018-0007-6

Fellmann, C., Hoffmann, T., Sridhar, V., Hopfgartner, B., Muhar, M., Roth, M., Lai, D. Y., Barbosa, I. A., Kwon, J. S., Guan, Y. et al. (2013). An optimized microRNA backbone for effective single-copy RNAi. *Cell Rep.* **5**, 1704-1713. doi:10.1016/j.celrep.2013.11.020

Ferrari, A., Veligodskiy, A., Berge, U., Lucas, M. S. and Kroschewski, R. (2008). ROCK-mediated contractility, tight junctions and channels contribute to the conversion of a preapical patch into apical surface during isochoric lumen initiation. *J. Cell Sci.* **121**, 3649-3663. doi:10.1242/jcs.018648

Friedl, P. and Gilmour, D. (2009). Collective cell migration in morphogenesis, regeneration and cancer. *Nat. Rev. Mol. Cell Biol.* **10**, 445-457. doi:10.1038/nrm2720

Friedl, P., Locker, J., Sahai, E. and Segall, J. E. (2012). Classifying collective cancer cell invasion. *Nat. Cell Biol.* **14**, 777-783. doi:10.1038/ncb2548

Gandalovičová, A., Vomastek, T., Rosel, D. and Brábek, J. (2016). Cell polarity signaling in the plasticity of cancer cell invasiveness. *Oncotarget* **7**, 25022-25049. doi:10.18632/oncotarget.7214

Gassama-Diagne, A., Yu, W., ter Beest, M., Martin-Belmonte, F., Kierbel, A., Engel, J. and Mostov, K. (2006). Phosphatidylinositol-3,4,5-trisphosphate regulates the formation of the basolateral plasma membrane in epithelial cells. *Nat. Cell Biol.* **8**, 963-970. doi:10.1038/ncb1461

Goranci-Buzhala, G., Mariappan, A., Gabriel, E., Ramani, A., Ricci-Vitiani, L., Buccarelli, M., D'Alessandris, Q. G., Pallini, R. and Gopalakrishnan, J. (2020). Rapid and efficient invasion assay of glioblastoma in human brain organoids. *Cell Rep.* **31**, 107738. doi:10.1016/j.celrep.2020.107738

Gracia, M., Theis, S., Proag, A., Gay, G., Benassayag, C. and Suzanne, M. (2019). Mechanical impact of epithelial-mesenchymal transition on epithelial morphogenesis in Drosophila. *Nat. Commun.* **10**, 2951. doi:10.1038/s41467-019-10720-0

Gudjonsson, T., Rønnov-Jessen, L., Villadsen, R., Rank, F., Bissell, M. J. and Petersen, O. W. (2002). Normal and tumor-derived myoepithelial cells differ in their ability to interact with luminal breast epithelial cells for polarity and basement membrane deposition. *J. Cell Sci.* **115**, 39-50. doi:10.1242/jcs.115.1.39

Han, Y. L., Pegoraro, A. F., Li, H., Li, K., Yuan, Y., Xu, G., Gu, Z., Sun, J., Hao, Y., Gupta, S. K. et al. (2020). Cell swelling, softening and invasion in a three-dimensional breast cancer model. *Nat. Phys.* **16**, 101-108. doi:10.1038/s41567-019-0680-8

Heino, J. and Massagué, J. (1989). Transforming growth factor-β switches the pattern of integrins expressed in MG-63 human osteosarcoma cells and causes a selective loss of cell adhesion to laminin. *J. Biol. Chem.* **264**, 21806-21811. doi:10.1016/S0021-9258(20)88255-6

Huang, W., Navarro-Serer, B., Jeong, Y. J., Chianchiano, P., Xia, L., Luchini, C., Veronese, N., Dowiak, C., Ng, T., Trujillo, M. A. et al. (2020). Pattern of invasion in human pancreatic cancer organoids is associated with loss of SMAD4 and clinical outcome. *Cancer Res.* **80**, 2804-2817. doi:10.1158/0008-5472.CAN-19-1523

Huber, W., Carey, V. J., Gentleman, R., Anders, S., Carlson, M., Carvalho, B. S., Bravo, H. C., Davis, S., Gatto, L., Girke, T. et al. (2015). Orchestrating high-throughput genomic analysis with Bioconductor. *Nat. Methods* **12**, 115-121. doi:10.1038/nmeth.3252

Ilina, O. and Friedl, P. (2009). Mechanisms of collective cell migration at a glance. *J. Cell Sci.* **122**, 3203-3208. doi:10.1242/jcs.036525

Ilina, O., Gritsenko, P. G., Syga, S., Lippoldt, J., La Porta, C. A. M., Chepizhko, O., Grosser, S., Vullings, M., Bakker, G.-J., Starruß, J. et al. (2020). Cell-cell adhesion and 3D matrix confinement determine jamming transitions in breast cancer invasion. *Nat. Cell Biol.* **22**, 1103-1115. doi:10.1038/s41556-020-0552-6

Ishizaki, T., Uehata, M., Tamechika, I., Keel, J., Nonomura, K., Maekawa, M. and Narumiya, S. (2000). Pharmacological properties of Y-27632, a specific inhibitor of rho-associated kinases. *Mol. Pharmacol.* **57**, 976-983.

Jass, J. R. (2007). Classification of colorectal cancer based on correlation of clinical, morphological and molecular features. *Histopathology* **50**, 113-130. doi:10.1111/j.1365-2559.2006.02549.x

Julien, S., Merino-Trigo, A., Lacroix, L., Pocard, M., Goéré, D., Mariani, P., Landron, S., Bigot, L., Nemati, F., Dartigues, P. et al. (2012). Characterization of a large panel of patient-derived tumor xenografts representing the clinical heterogeneity of human colorectal cancer. *Clin. Cancer Res.* **18**, 5314-5328. doi:10.1158/1078-0432.CCR-12-0372

Jung, H.-Y., Fattet, L., Tsai, J. H., Kajimoto, T., Chang, Q., Newton, A. C. and Yang, J. (2019). Apical-basal polarity inhibits epithelial-mesenchymal transition and tumour metastasis by PAR-complex-mediated SNAI1 degradation. *Nat. Cell Biol.* **21**, 359-371. doi:10.1038/s41556-019-0291-8

Koga, Y., Song, H., Chalmers, Z. R., Newberg, J., Kim, E., Carrot-Zhang, J., Piou, D., Polak, P., Abdulkadir, S. A., Ziv, E. et al. (2020). Genomic profiling of prostate cancers from men with African and European Ancestry. *Clin. Cancer Res.* **26**, 4651-4660. doi:10.1158/1078-0432.CCR-19-4112

Kroepfl, J. F. and Gardinier, M. V. (2001). Mutually exclusive apicobasolateral sorting of two oligodendroglial membrane proteins, proteolipid protein and myelin/oligodendrocyte glycoprotein, in Madin-Darby canine kidney cells. *J. Neurosci. Res.* **66**, 1140-1148. doi:10.1002/jnr.10035

Kryvenko, O. N., Chitale, D. A., Yoon, J., Arias-Stella, J., Meier, F. A. and Lee, M. W. (2013). Precursor Lesions of Mucinous Carcinoma of the Breast: Analysis of 130 Cases. *Am. J. Surg. Pathol.* **37**, 1076-1084. doi:10.1097/PAS.0b013e31828de420

Libanje, F., Raingeaud, J., Luan, R., Thomas, Z., Zajac, O., Veiga, J., Marisa, L., Adam, J., Boige, V., Malka, D. et al. (2019). ROCK2 inhibition triggers the collective invasion of colorectal adenocarcinomas. *EMBO J.* **38**, e99299. doi:10.15252/embj.201899299

Liu, K. D., Datta, A., Yu, W., Brakeman, P. R., Jou, T.-S., Matthay, M. A. and Mostov, K. E. (2007). Rac1 is required for reorientation of polarity and lumen formation through a PI 3-kinase-dependent pathway. *Am. J. Physiol. Renal. Physiol.* **293**, F1633-F1640. doi:10.1152/ajprenal.00053.2007

Margadant, C. and Sonnenberg, A. (2010). Integrin-TGF-beta crosstalk in fibrosis, cancer and wound healing. *EMBO Rep.* **11**, 97-105. doi:10.1038/embor.2009.276

Margaron, Y., Nagai, T., Guyon, L., Kurzawa, L., Morel, A.-P., Pinheiro, A., Blanchoin, L., Reyal, F., Puisieux, A. and Théry, M. (2019). Biophysical properties of intermediate states of EMT outperform both epithelial and mesenchymal states. *bioRxiv*, 797654 doi:10.1101/797654

Negri, F. V., Wotherspoon, A., Cunningham, D., Norman, A. R., Chong, G. and Ross, P. J. (2005). Mucinous histology predicts for reduced fluorouracil responsiveness and survival in advanced colorectal cancer. *Ann. Oncol.* **16**, 1305-1310. doi:10.1093/annonc/mdi244

Nieto, M. A., Huang, R. Y.-J., Jackson, R. A. and Thiery, J. P. (2016). EMT: 2016. *Cell* **166**, 21-45. doi:10.1016/j.cell.2016.06.028

Okuyama, H., Kondo, J., Sato, Y., Endo, H., Nakajima, A., Piulats, J. M., Tomita, Y., Fujiwara, T., Itoh, Y., Mizoguchi, A. et al. (2016). Dynamic change of polarity in primary cultured spheroids of human colorectal adenocarcinoma and its role in metastasis. *Am. J. Pathol.* **186**, 899-911. doi:10.1016/j.ajpath.2015.12.011

Padmanaban, V., Krol, I., Suhail, Y., Szczerba, B. M., Aceto, N., Bader, J. S. and Ewald, A. J. (2019). E-cadherin is required for metastasis in multiple models of breast cancer. *Nature* **573**, 439-444. doi:10.1038/s41586-019-1526-3

Padmanaban, V., Grasset, E. M., Neumann, N. M., Fraser, A. K., Henriet, E., Matsui, W., Tran, P. T., Cheung, K. J., Georgess, D. and Ewald, A. J. (2020). Organotypic culture assays for murine and human primary and metastatic-site tumors. *Nat. Protoc.* **15**, 2413-2442. doi:10.1038/s41596-020-0335-3

Peterson, L. J., Rajfur, Z., Maddox, A. S., Freel, C. D., Chen, Y., Edlund, M., Otey, C. and Burridge, K. (2004). Simultaneous stretching and contraction of stress fibers in vivo. *Mol. Biol. Cell.* **15**, 3497-3508. doi:10.1091/mbc.e03-09-0696

Ricard-Blum, S. (2011). The collagen family. *Cold Spring Harb. Perspect. Biol.* **3**, a004978. doi:10.1101/cshperspect.a004978

Roy, P., Canet-Jourdan, C., Annereau, M., Zajac, O., Gelli, M., Broutin, S., Mercier, L., Paci, A., Lemare, F., Ducreux, M. et al. (2017). Organoids as preclinical models to improve intraperitoneal chemotherapy effectiveness for colorectal cancer patients with peritoneal metastases: Preclinical models to improve HIPEC. *Int. J. Pharm.* **531**, 143-152. doi:10.1016/j.ijpharm.2017.07.084

Saito, Y., Desai, R. R. and Muthuswamy, S. K. (2018). Reinterpreting polarity and cancer: the changing landscape from tumor suppression to tumor promotion. *Biochim. Biophys. Acta Rev. Cancer* **1869**, 103-116. doi:10.1016/j.bbcan.2017.12.001

Sato, T. and Clevers, H. (2013). Growing self-organizing mini-guts from a single intestinal stem cell: mechanism and applications. *Science* **340**, 1190-1194. doi:10.1126/science.1234852

Sheppard, D., Cohen, D. S., Wang, A. and Busk, M. (1992). Transforming growth factor beta differentially regulates expression of integrin subunits in guinea pig airway epithelial cells. *J. Biol. Chem.* **267**, 17409-17414. doi:10.1016/S0021-9258(18)41941-2

Spaderna, S., Schmalhofer, O., Hlubek, F., Berx, G., Eger, A., Merkel, S., Jung, A., Kirchner, T. and Brabletz, T. (2006). A transient, EMT-linked loss of basement membranes indicates metastasis and poor survival in colorectal cancer. *Gastroenterology* **131**, 830-840. doi:10.1053/j.gastro.2006.06.016

Subramanian, A., Tamayo, P., Mootha, V. K., Mukherjee, S., Ebert, B. L., Gillette, M. A., Paulovich, A., Pomeroy, S. L., Golub, T. R., Lander, E. S. et al. (2005). Gene set enrichment analysis: a knowledge-based approach for interpreting genome-wide expression profiles. *Proc. Natl. Acad. Sci. USA* **102**, 15545-15550. doi:10.1073/pnas.0506580102

Thorpe, D., Stringer, A. and Butler, R. (2013). Chemotherapy-induced mucositis: the role of mucin secretion and regulation, and the enteric nervous system. *Neurotoxicology* **38**, 101-105. doi:10.1016/j.neuro.2013.06.007

Tsai, J.-H., Jeng, Y.-M., Yuan, C.-T., Lin, Y.-L., Cheng, M.-L. and Liau, J.-Y. (2019). Traditional serrated pathway–associated colorectal carcinoma: morphologic reappraisal of serrated morphology, tumor budding, and identification of frequent PTEN alterations. *Am. J. Surg. Pathol.* **43**, 1042-1051. doi:10.1097/PAS.0000000000001274

Tusher, V. G., Tibshirani, R. and Chu, G. (2001). Significance analysis of microarrays applied to the ionizing radiation response. *Proc. Natl. Acad. Sci. USA* **98**, 5116-5121. doi:10.1073/pnas.091062498

Tuveson, D. and Clevers, H. (2019). Cancer modeling meets human organoid technology. *Science* **364**, 952-955. doi:10.1126/science.aaw6985

Vlachogiannis, G., Hedayat, S., Vatsiou, A., Jamin, Y., Fernández-Mateos, J., Khan, K., Lampis, A., Eason, K., Huntingford, I., Burke, R. et al. (2018). Patient-derived organoids model treatment response of metastatic gastrointestinal cancers. *Science* **359**, 920-926. doi:10.1126/science.aao2774

Wellner, U., Schubert, J., Burk, U. C., Schmalhofer, O., Zhu, F., Sonntag, A., Waldvogel, B., Vannier, C., Darling, D., zur Hausen, A. et al. (2009). The EMT-activator ZEB1 promotes tumorigenicity by repressing stemness-inhibiting microRNAs. *Nat. Cell Biol.* **11**, 1487-1495. doi:10.1038/ncb1998

Wolf, K. and Friedl, P. (2011). Extracellular matrix determinants of proteolytic and non-proteolytic cell migration. *Trends Cell Biol.* **21**, 736-744. doi:10.1016/j.tcb.2011.09.006

Wosen, J. E., Mukhopadhyay, D., Macaubas, C. and Mellins, E. D. (2018). Epithelial MHC class II expression and its role in antigen presentation in the gastrointestinal and respiratory tracts. *Front. Immunol.* **9**, 2144. doi:10.3389/fimmu.2018.02144

Yao, Y., Xu, X., Yang, L., Zhu, J., Wan, J., Shen, L., Xia, F., Fu, G., Deng, Y., Pan, M. et al. (2020). Patient-derived organoids predict chemoradiation responses of locally advanced rectal cancer. *Cell Stem Cell* **26**, 17-26.e6. doi:10.1016/j.stem.2019.10.010

Yu, W., Datta, A., Leroy, P., O'Brien, L. E., Mak, G., Jou, T.-S., Matlin, K. S., Mostov, K. E. and Zegers, M. M. P. (2005). β1-integrin orients epithelial polarity via Rac1 and laminin. *MBoC* **16**, 433-445. doi:10.1091/mbc.e04-05-0435

Zajac, O., Raingeaud, J., Libanje, F., Lefebvre, C., Sabino, D., Martins, I., Roy, P., Benatar, C., Canet-Jourdan, C., Azorin, P. et al. (2018). Tumour spheres with inverted polarity drive the formation of peritoneal metastases in patients with hypermethylated colorectal carcinomas. *Nat. Cell Biol.* **20**, 296-306. doi:10.1038/s41556-017-0027-6

Zambruno, G., Marchisio, P. C., Marconi, A., Vaschieri, C., Melchiori, A., Giannetti, A. and De Luca, M. (1995). Transforming growth factor-beta 1 modulates beta 1 and beta 5 integrin receptors and induces the de novo expression of the alpha v beta 6 heterodimer in normal human keratinocytes: implications for wound healing. *J. Cell Biol.* **129**, 853-865. doi:10.1083/jcb.129.3.853

Zanoni, M., Cortesi, M., Zamagni, A., Arienti, C., Pignatta, S. and Tesei, A. (2020). Modeling neoplastic disease with spheroids and organoids. *J. Hematol. Oncol.* **13**, 97. doi:10.1186/s13045-020-00931-0

Zou, K. H., O'Malley, A. J. and Mauri, L. (2007). Receiver-operating characteristic analysis for evaluating diagnostic tests and predictive models. *Circulation* **115**, 654-657. doi:10.1161/CIRCULATIONAHA.105.594929

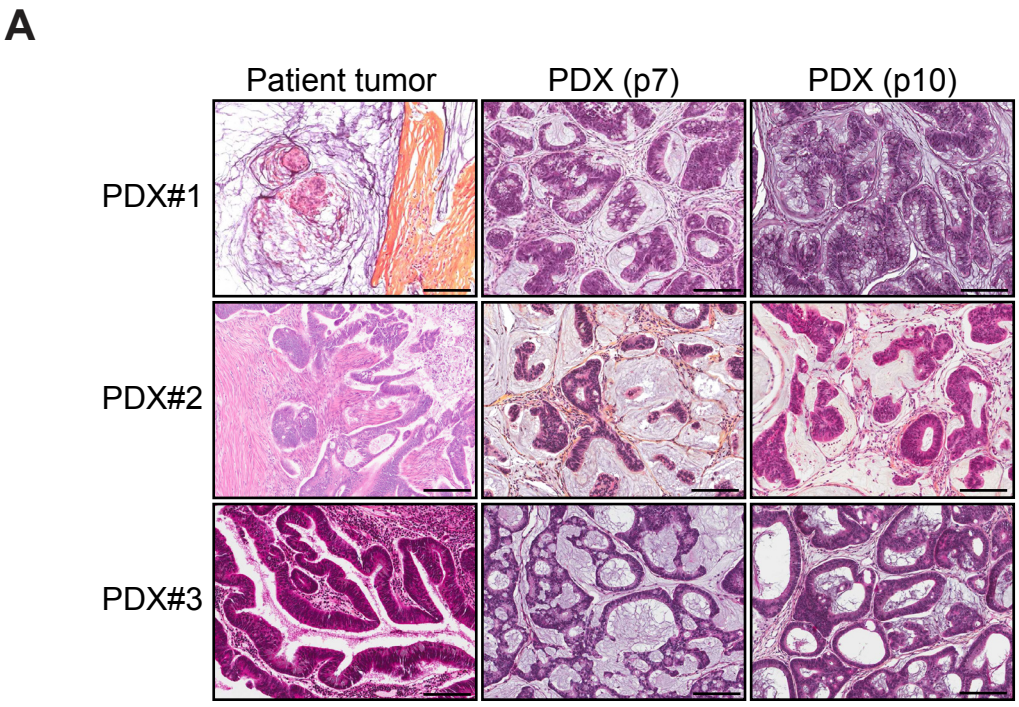

Fig. S1.

(A) HES staining of patient tumors that were used to make PDX and HES staining of 2 different passages of PDX (p7 and p10). Scale bar=250µm.

(B) Organoids from PDX#1, #2 and #3 fixed after 3 days in suspension and stained with GM130 (Golgi apparatus), ezrin and DAPI (blue). Scale bar=50µm.

(C) Quantifications of PDX#1, #2 and #3 organoids' polarity after 3 days in in suspension for n=3 inde-pendent experiments.

Data are represented as mean±s.e.m.

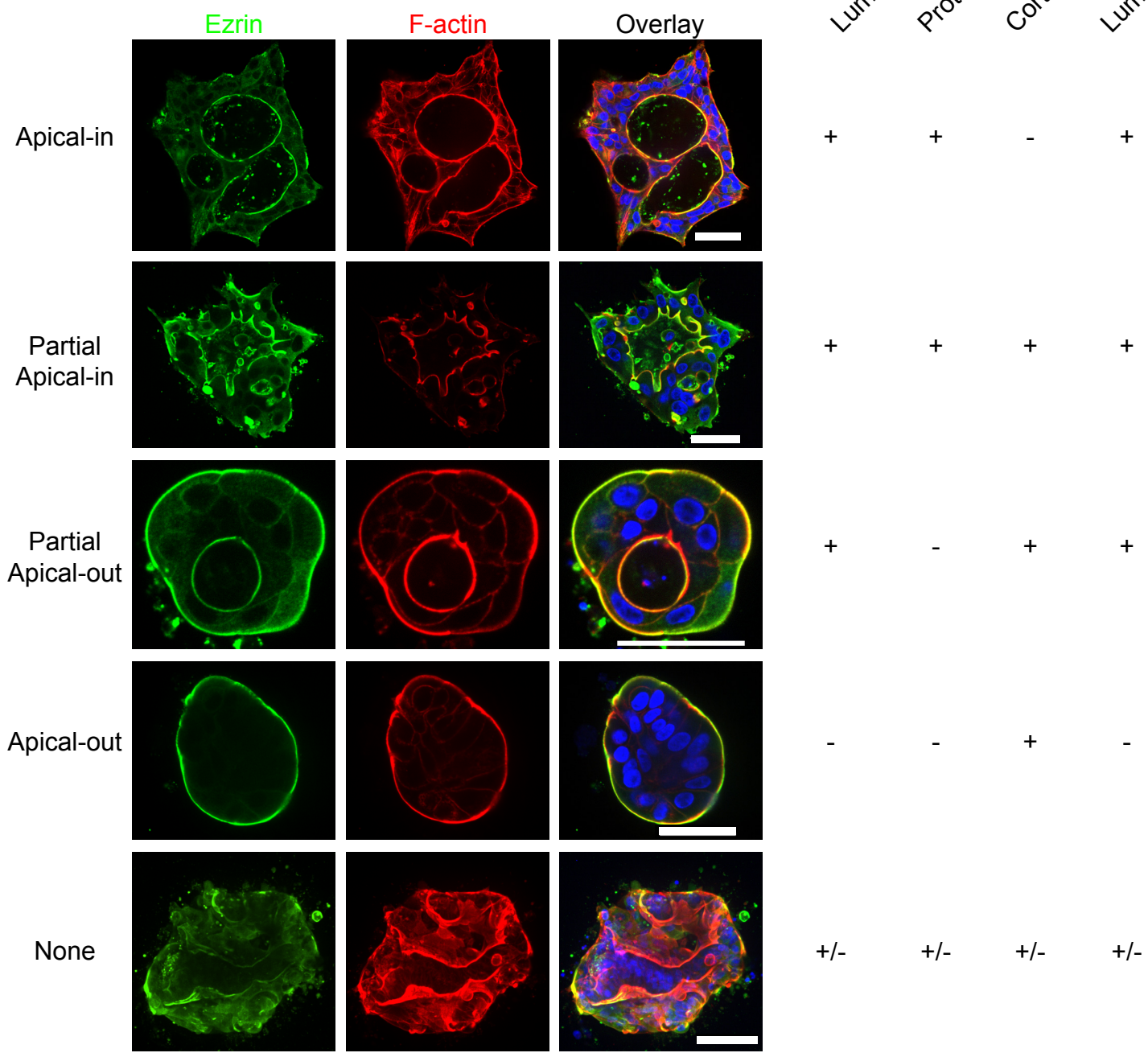

Fig. S2. Representative images of organoids polarity after 3 to 6 days in collagen-I gels and immunostained for ezrin, F-actin and DAPI (blue). Various topologies are observed and quantified based on morphological characteristics and localization of ezrin. Scale bar=50µm.

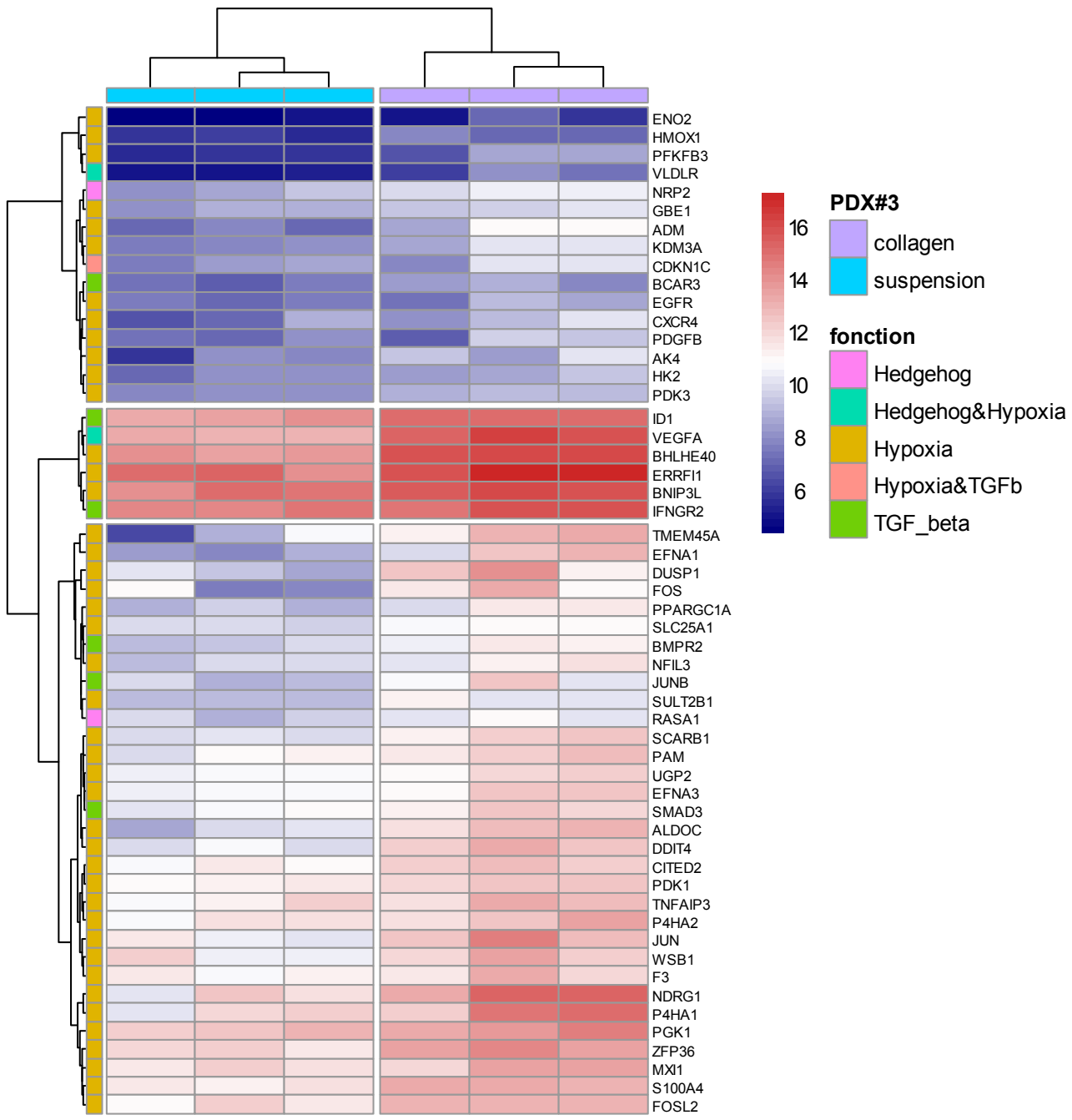

Fig. S3. (corresponding to supplementary table 1):

In GSEA collagen-I PDX#3 specific signature, 54 genes were found up regulated with a fold change over 2 and reclassified experimental groups.

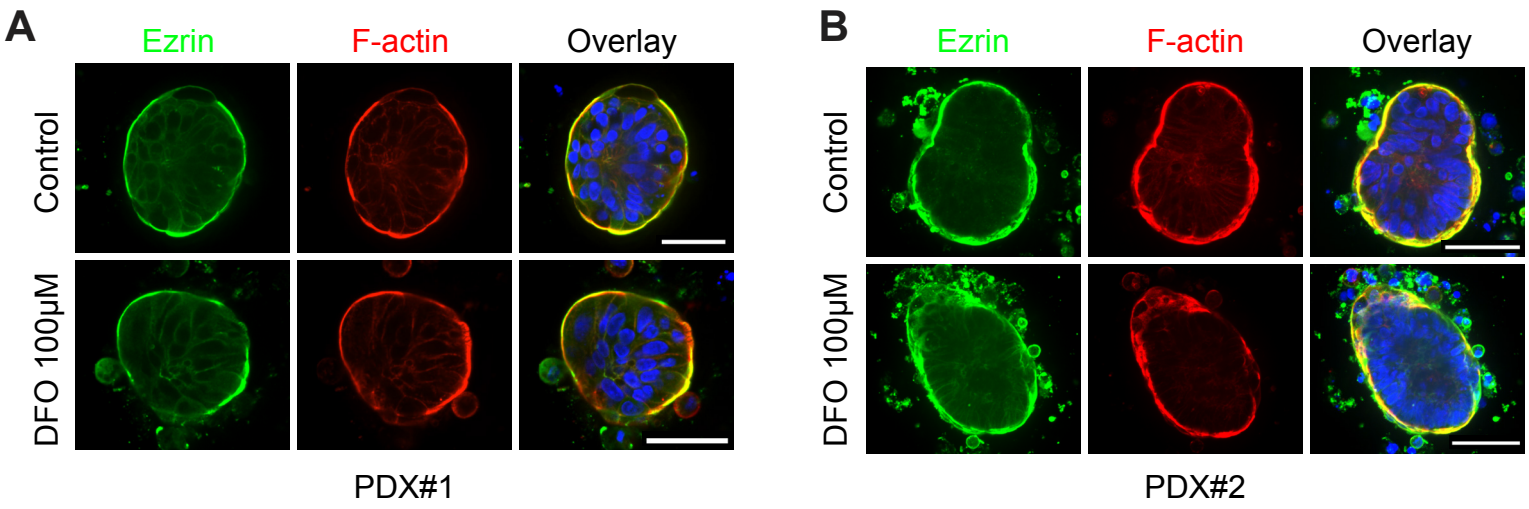

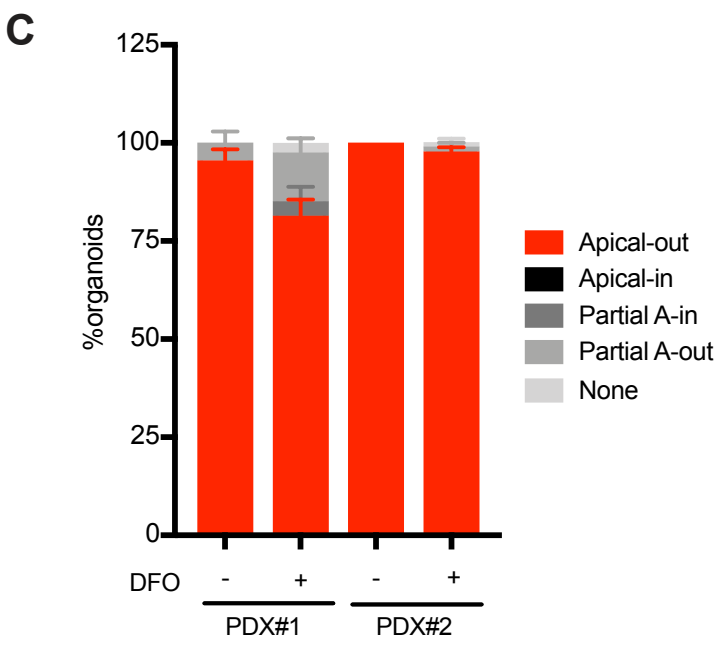

Fig. S4. (A,B) Organoids from PDX#1 (A) and #2 (B) treated with DFO (100µM for 3 days) in collagen-I gels and immunostained for ezrin, F-actin and DAPI (blue). Scale bar=50µm.
(C) Quantifications of PDX#1 and PDX#2 organoids' phenotypes after DFO treatment (n=3 experiments with 88 and 73 PDX#1 organoids counted for control and DFO conditions respectively, and 90 PDX#2 organoids for each condition).
Data are represented as mean±s.e.m.

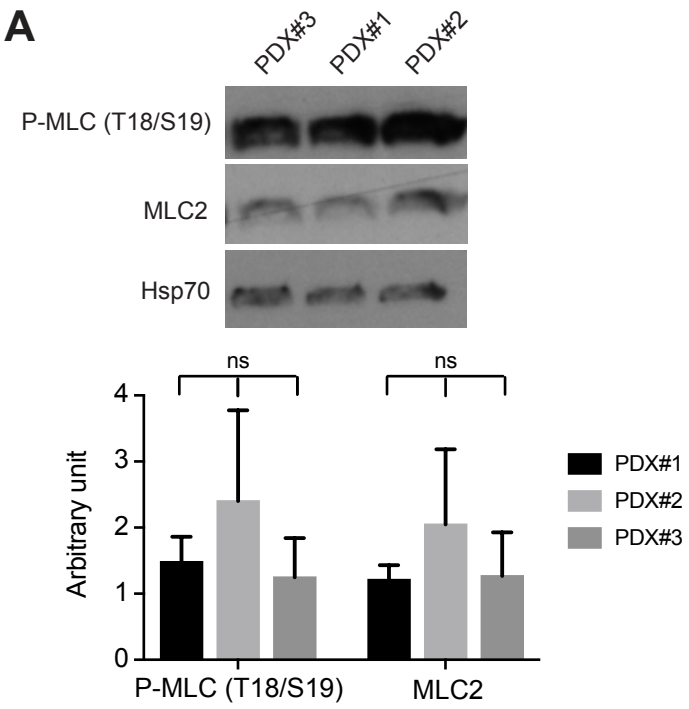
A
PDX#3
PDX#1
PDX#2
P-MLC (T18/S19)
MLC2
Hsp70
ns
ns
Arbitrary unit
0
1
2
3
4
P-MLC (T18/S19)
MLC2
PDX#1
PDX#2
PDX#3

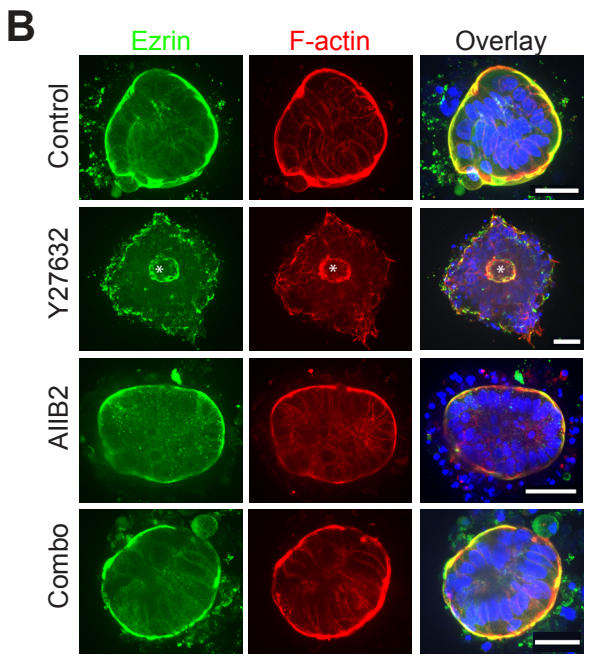
B
Ezrin
F-actin
Overlay
Control
Y27632
AIIB2
Combo

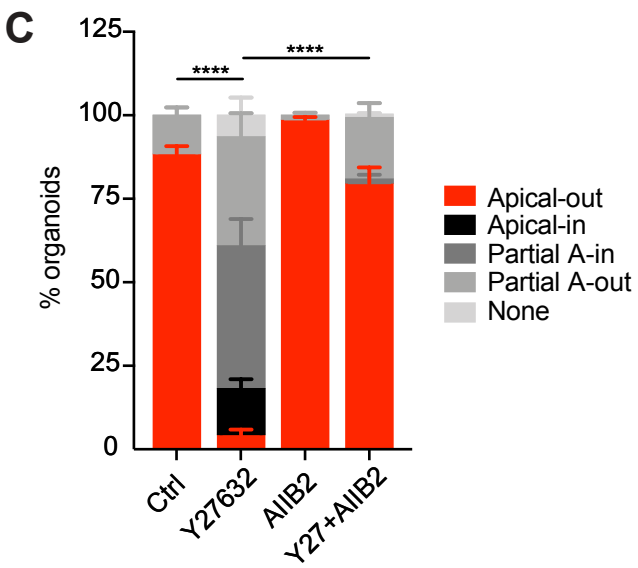
C
125
100
75
50
25
0
% organoids
****
****
Apical-out
Apical-in
Partial A-in
Partial A-out
None
Ctrl
Y27632
AIIB2
Y27+AIIB2

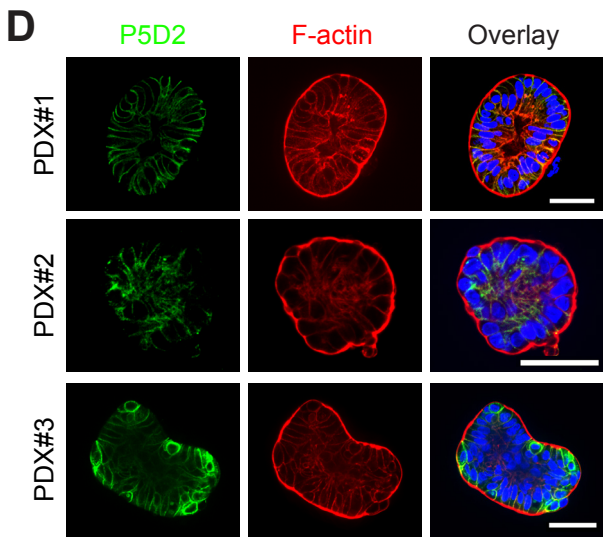
D
P5D2
F-actin
Overlay
PDX#1
PDX#2
PDX#3

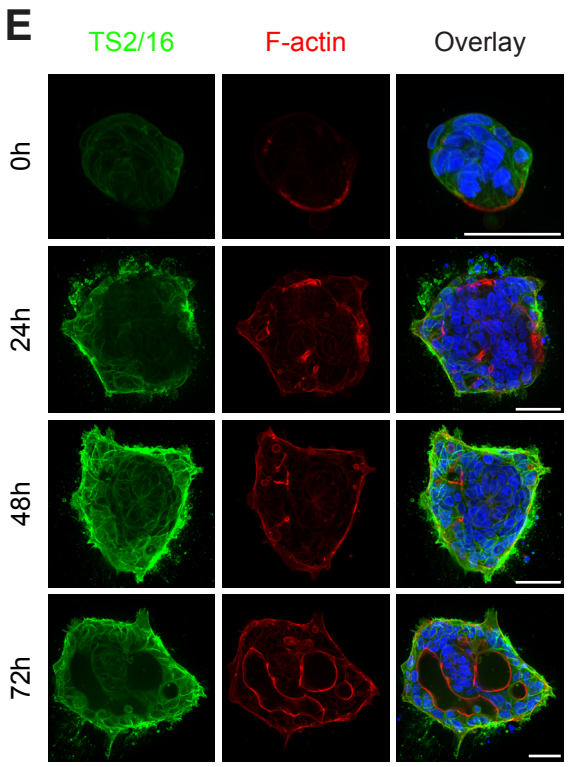
E
TS2/16
F-actin
Overlay
0h
24h
48h
72h

Fig. S5.

(A) A) Representative images of western blots for phosphorylated myo light chain (P-MLC), myosin light chain 2 (MLC2) and Hsp70 of PDX#1, PDX#2 and PDX#3 organoids after 3 days in suspension (A) and quantifi-cation (B) expressed as the ratio of P-MLC or MLC2 over Hsp70 signal (n=3 experiments).

(B) B) PDX#1 ganoids immunostained for ezrin, F-actin and DAPI (blue) after 6 days in collagen-I gels treated with Y27632 (25µM), AIIB2
(1µg/mL) or the two combined (combo).
*=lumen.

(C) C) Quantifications of PDX#1 ganoids polarity after Y27632, AIIB2 or combo (Y27632+AIIB2) treatments (n=5 experiments with 145, 141, 146 and 141 organoids counted in total for control, Y27632, AIIB2 and Y27632+AIIB2 conditions respectively).

(D) D) ganoids from PDX#1, PDX#2 and PDX#3 immunostained for integrin-β1 (P5D2), F-actin and DAPI (blue) after 3 days in suspension.

(E) E) PDX#3 ganoids immunostained for Integrin-β1 (TS2/16), F-actin and DAPI in suspension (0h) and 24h, 48h and 72h in collagen-I gel. Scale bar=50µm.

Statistics: unpaired two-tailed t-tests were performed for panel A, one-way ANOVA for panel C with ****P<0.0001. Data are represented as mean±s.e.m.

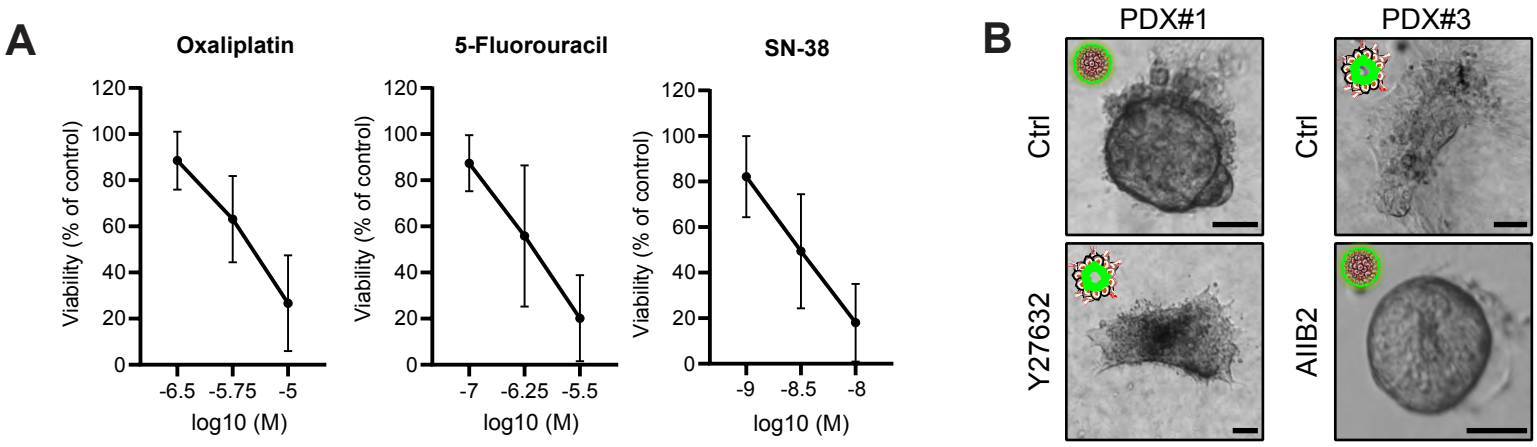

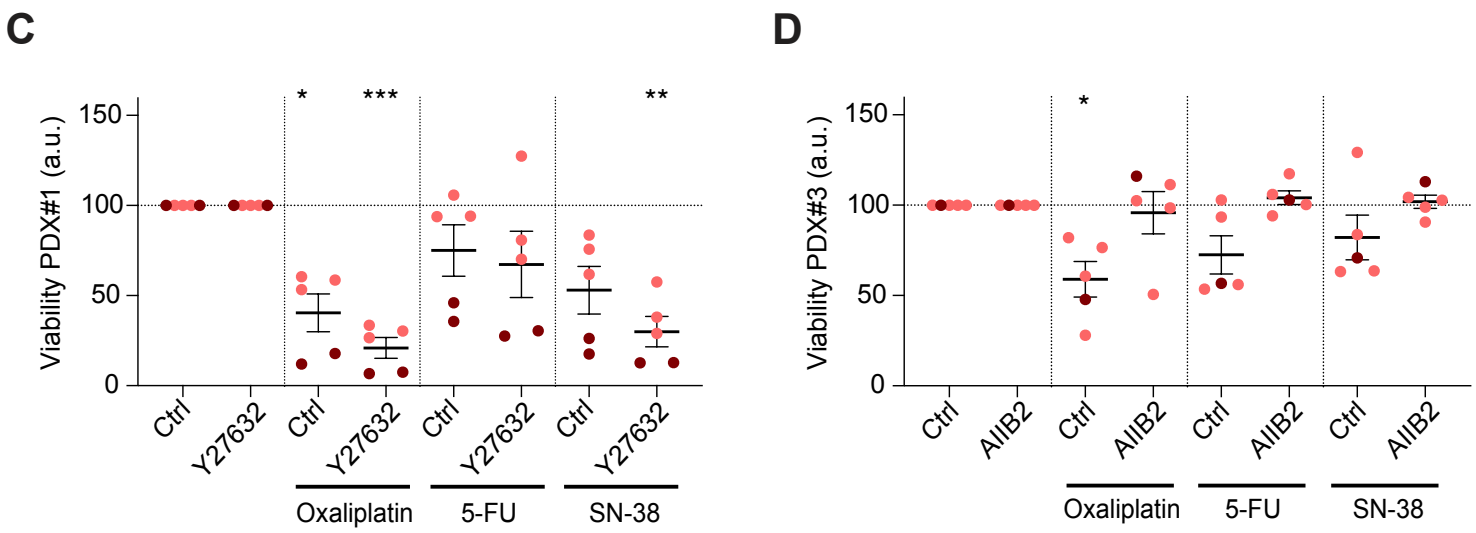

Fig. S6.

(A) Average viability (measured as ATP levels quantification) as a function of chemotherapy concentration for a cohort of 25 patients CRC organoids treated with Oxaliplatin, 5-Fluorouracil and Irinotecan (SN-38), used to determine the IC70. Error bars are SD.

(B) Representative bright field images of PDX#1 in control condition (Ctrl) or treated with Y27632 (25µM) (left panel) and PDX#3 in control condition or treated with AIIB2 (1µg/mL) (right panel). Scale bar=50µm.

(C,D) Viability of PDX#1 (C) and PDX#3 (D) organoids in wild-type (Ctrl) or treated with Y27632 (25 µM), then incubated for 2 days (orange dots) or 4-5 days (red dots) with Oxaliplatin (10 µM), 5-Fluorou-racil (5-FU, 1.8µM) or Irinotecan (SN-38, 6.10-3 µM). Viability is quantified as the average ATP levels in triplicates, normalized by ATP levels of the control condition (either Ctrl, AIIB2 or Y27632) (see Material and Methods).

Statistics: one-way ANOVA for C and D with ***P<0.001, **P<0.01, *P<0.05.

Data are represented as mean±s.e.m.

Table S1. Genes regulated by collagen-I in PDX#3.

gene	PDX#3 ratio Coll/Susp
C3	45,89
KCTD11	14,89
CLIC3	12,91
GPER1	11,85
LRP1	10,43
ALOX15B	9,51
CA9	8,36
SORL1	8,09
SCD	7,80
CEMIP	7,34
VEGFA	6,79
AHNAK	6,74
HSD3B1	6,13
FLNB	5,94
DDIT4	5,87
SERPINA1	5,79
GAL3ST1	5,74
SLC22A18	5,58
MYO7B	5,44
SYNPO	5,33
NPY4R	4,89
PRKAA2	4,87
C6orf223	4,82
BHLHE40	4,76
PRAP1	4,69
CA2	4,47
PRKCDBP	4,27
NOXO1	4,21
ATP2B4	4,16
CDC42BPB	3,89
AGRN	3,88
ACSS2	3,85
FAM213A	3,43
DYNC1H1	3,43
QSER1	3,43
S100A4	3,35
TRIB3	3,23
PTPRF	3,22
TRIB2	3,07
MSL1	3,06
HMOX1	3,06
DUSP6	3,01
PRSS12	2,99
TFF3	2,98
AMOT	2,95
PIK3C2B	2,95
PLA2R1	2,95
ITGB4	2,93
NBEAL1	2,93
TMEM135	2,87
ID1	2,82
IGF2R	2,82
GTF2IRD2B	2,73
LAMA5	2,73
ZFAND3	2,71

gene	PDX#3 ratio Coll/Susp
BAZ2A	2,70
HIST1H2AC	2,69
PARP14	2,68
CIDEB	2,66
FOXN3	2,65
DOCK4	2,60
MTRNR2L9	2,56
KAT2B	2,56
EYA4	2,55
UGT2A3	2,52
MTRNR2L6	2,51
TLK1	2,50
ELMSAN1	2,50
TANC1	2,48
ANO6	2,46
PER2	2,45
SLC41A2	2,45
SPG11	2,43
PITX2	2,39
VPS13C	2,38
PRPF8	2,35
ARL4A	2,30
PTK6	2,29
NBAS	2,27
PTGR1	2,22
CCL14	2,21
MAN2A1	2,20
SEC24A	2,19
CST3	2,19
SLC25A1	2,13
FZD5	2,13
NAT8	2,12
PAK2	2,12
KDM5B	2,11
SECISBP2L	2,11
PSD4	2,08
ACSL3	2,07
PDK3	2,07
MIA3	2,04
PGAM1	2,03
EPAS1	2,02
RPL29	2,00
PSMD1	-2,01
C20orf196	-2,03
COL3A1	-2,05
RRP7A	-2,05
MED24	-2,08
SETD7	-2,08
TTC13	-2,10
GLE1	-2,10
MBTPS2	-2,12
DHDDS	-2,12
TSFM	-2,13
SLC20A2	-2,16
CASP2	-2,17

gene	PDX#3 ratio Coll/Susp
RGS2	-2,18
NT5DC2	-2,24
OGFOD1	-2,26
FAM109B	-2,31
SLC37A3	-2,32
C16orf62	-2,32
KLHL18	-2,37
MRRF	-2,37
IPO9	-2,38
ZAK	-2,39
MFSD1	-2,42
ITGAE	-2,42
L3MBTL2	-2,46
HSPA14	-2,49
NUBPL	-2,51
SUPT16H	-2,58
SLC39A8	-2,61
CHID1	-2,64
REEP4	-2,68
PADI2	-2,74
HACD3	-2,78
CMSS1	-2,82
SLC25A32	-2,91
NMU	-2,95
STEAP4	-3,05
CLPB	-3,08
RTKN2	-3,10
MTHFD1	-3,27
DDIAS	-3,47
CACNB4	-3,49
TRMT1	-3,59
ELOVL7	-3,66
RCC1	-3,81
APOBEC3B	-3,84
FANCI	-4,09
REP15	-4,47
CORO1A	-4,82
TACC1	-4,85
CDCA7L	-5,00
COCH	-5,40
CGB1	-6,28
TMEM173	-6,45
CGB	-6,76
CGB8	-7,91
SLC43A1	-9,08
REG1B	-11,66
HEPACAM2	-20,39
REG1A	-29,72

Table S2. Genes regulated by collagen-I in PDX#1 and PDX#2.

gene	PDX#1 and PDX#2 ratio Coll/Susp
CCL20	34,74
UBD	23,45
CXCL8	12,68
MMP7	8,85
PI3	7,25
TNFAIP3	5,68
GLIPR1	5,65
TNFRSF9	5,24
BIRC3	4,88
PLAU	4,84
NDUFA4L2	4,41
CXCL1	4,30
SPRR2A	4,12
CXCL11	4,00
IL1B	3,91
IL32	3,46
IL1A	3,41
ARRDC3	3,08
KRT6A	3,03
S100A3	2,78
SERPINB9	2,73
DCBLD2	2,70
MAOB	2,69
VNN1	2,60
IFI6	2,56
CLIC3	2,33
LAMC2	2,22
SDC4	2,20
GUCA2A	2,20
B3GALT5	2,15
TGM2	2,13
BHLHE40	2,09
ADGRF1	2,08
SULT1B1	2,08
CD83	1,96
IFNGR2	1,96